Investigation of the Charge Density Wave Ordering in Intercalated $ZrTe_2$ materials

A thesis Submitted towards the partial fullfilment of
BS-MS dual degree programme
by

DIVYA YADAV

DATE: 27th March 2025

under the supervision of

Prof. Surjeet Singh

Indian Institute of Science Education and Research Pune

from May 2024 to Mar 2025

INDIAN INSTITUTE OF SCIENCE EDUCATION AND RESEARCH PUNE

Certificate

This is to certify that this dissertation entitled '**Investigation of the Charge Density wave ordering in Intercalated $ZrTe_2$ materials**' towards the partial fulfillment of the BS-MS dual degree programme at the Indian Institute of Science Education and Research, Pune represents study/work carried out by Divya Yadav at IISER Pune under the supervision of Professor Surjeet Singh, during the academic year 2024-2025.

Supervisor:
Prof. Surjeet Singh
Department of Physics
IISER Pune

Student:
Divya yadav
20201074
BS-MS, IISER Pune

Declaration

I hereby declare that the matter embodied in the report entitled " **Investigation of the Charge Density Wave Ordering in Intercalated $ZrTe_2$ materials** " are the result of the work carried out by me at the Department of Physics, Indian Institute of Science Education and Research (IISER) Pune, under the supervision of Prof. Surjeet Singh, and the same has not been submitted elsewhere for any other degree. Wherever others contribute, every effort is made to indicate this clearly, with due reference to the literature and acknowledgment of collaborative research and discussions.

DIVYA YADAV
20201074

Acknowlegements

I would like to express my sincere appreciation to Prof. Surjeet Singh for his consistent guidance and support throughout my Master's thesis journey. His expertise and valuable feedback have been crucial in shaping my academic and research journey, providing a robust foundation for my work in the field of correlated systems.

I am also grateful to Professor Emeritus Srinivasan Ramakrishnan, who served as my thesis advisor. His expertise and insightful discussions have significantly enhanced the quality of my research.

I am also grateful to Prof. Arumugam Thamizhavel for his invaluable assistance with the low-temperature magnetoresistance measurements crucial to successfully completing the experimental work presented in this thesis.

I am highly grateful to my lab members, Sagar Dada, Nashra Di, Ankit Bhaiya, Dinesh Bhaiya, and Pankaj Bhaiya, for their mentorship and for teaching me essential experimental techniques for performing experimental work in the lab. I would like to extend my heartfelt gratitude to Luminita Ma'am. Her insights, expertise, and advice regarding crystal growth have greatly helped with my successful crystal growths, which were crucial for the completion of this work.I would like to extend my sincere appreciation to Sagar Bhaiya and Prabhu bhaiya for the insightful discussions, which have significantly enhanced my understanding of research. I am thankful to Dinesh Bhaiya for his valuable insights into instrumentation and for teaching me essential skills related to it. I extend my heartful gratitude to Prabhu bhaiya, Pankaj Bhaiya, Meghna, Shagun, Vishak, Arindam, and Ankit Bhaiya for making the lab a lively and supportive workplace.

I extend my heartfelt gratitude to Nilesh Sir, Sudhir Sir, Anil Sir, and Karthikeyan for their invaluable technical expertise, which played a pivotal role in overcoming the complexities of laboratory work and ensuring its smooth progression.

I would like to express my heartfelt gratitude to Nidhi, Kavan, and Shijil for their unwavering support and belief in me. Their encouragement has been fundamental to my growth. My heartfelt gratitude to Brijesh and Anshul for turning ordinary days into truly amazing moments. Subiksha, Devadarshini, Anuja and Akanksha have greatly enriched my life beyond academics, creating memorable and joyful moments.

I would like to convey my sincere appreciation to my parents and grandmother for their unwavering guidance and support. Their thoughtful advice and steadfast encouragement have

profoundly shaped my pursuits. Additionally, I wish to acknowledge the valuable companionship and support of my cousins and siblings, which has made my journey more enriching.

I'm deeply grateful for the support, encouragement, and guidance from all the wonderful individuals who made this thesis possible.

Abstract

Superconductivity (SC) and charge-density-wave (CDW) ordering are correlated electronic phases whose coexistence in certain materials has been a subject of significant interest. In general, the suppression of CDW–either through chemical doping or external pressure–can lead to the emergence of SC at low temperatures. The interplay between these phenomena has been debated for decades and is considered highly material-dependent. Transition-metal dichalcogenides (TMDCs), MX_2 (where M is a transition metal and X is a chalcogen), often exhibit CDW ordering or are proximate to CDW phases. However, the question of whether SC can be induced in these materials by suppressing CDW ordering has not been thoroughly explored. In this work, we investigate $ZrTe_2$, a member of the TMDC family. While pristine $ZrTe_2$ does not exhibit CDW ordering, Ni-intercalated $ZrTe_2$ has been reported to show CDW ordering at 287 K alongside superconductivity at 4.1 K. To further understand the competing phases in this system, we conducted a systematic study of the transport properties of Cr_xZrTe_2 (i.e., Cr-intercalated $ZrTe_2$. Additionally, $Ni_{0.04}ZrTe_2$ was analyzed to gain insights into the nature of CDW ordering and the structural changes induced by Ni intercalation. This study employs a home-built resistivity measurement setup capable of scanning temperatures from 4.3 K to 295 K using the temperature gradient of a helium-storage dewar. The thesis is divided into two parts: the first focuses on the design and validation of the low-temperature resistivity setup, while the second investigates intercalated $ZrTe_2$ systems. We synthesized Cr_xZrTe_2 (for $x = 0.25$–0.45), optimizing crystal growth conditions for each composition, and characterized them by measuring their temperature-dependent electrical resistivity (in some cases in-field measurements using a commercial transport measurement system is also carried out). These results provide a foundation for future anisotropic studies of Cr_xZrTe_2 to further unravel the complex magnetic interactions and competing electronic phases in these systems.

Contents

List of Figures

Chapter 1

Introduction

Layered transition metal dichalcogenides are quasi-2D materials with a general composition of MX_2 (where M is a transition metal, X is a chalcogen). Transition-metal dichalcogenides (TMDCs) exhibit a wide range of correlation effects, including charge density waves (CDW), superconductivity (SC), and long-range magnetic ordering. Further, some of these materials are known to exhibit coexistence of superconductivity and charge density wave. Recently, there has been a heightened interest in these materials due to their uncommon physical properties and relevance in quantum Information, spintronic devices, and various other photonic and optoelectronic applications.

Several previous studies have reported the coexistence of SC and CDW in transition metal dichalcogenides. However, group IV ditellurides have not been observed to exhibit CDW ordering in their bulk forms. A recent report suggests that $Ni_{0.04}ZrTe_2$ (i.e., 4% Ni intercalated $ZrTe_2$) potentially exhibits CDW ordering at 287 K alongside superconductivity below a critical temperature (T_C) of 4.1 K [6]. A more detailed investigation into the origin and characteristics of the CDW induced by Ni intercalation is needed. Additionally, it has been observed that upon intercalation of chromium in $TiTe_2$, the material exhibits CDW ordering and spin-glass behavior at low temperatures [2]. Further, recent reports on the magnetic properties of Cr-intercalated $ZrTe_2$ have revealed that $ZrTe_2$ similarly demonstrates spin-glass behavior over the identical intercalation concentrations as $TiTe_2$ [24]. However, a systematic exploration of the resistivity changes following the intercalation of chromium in $ZrTe_2$ is still lacking.

In this thesis, a thorough study of transport properties of the Cr_xZrTe_2 system is carried out to obtain a better understanding of the competing phases in this material. Moreover, we further aim to investigate the $Ni_{0.04}ZrTe_2$ system to verify the previous claim of the coexistence of CDW ordering and SC. The primary characterization tool used for charge density waves is often the presence of an anomaly in the measured resistivity at the CDW ordering, therefore, as part of this work, we have set up a slide-in type resistivity measurement system that utilizes the temperature gradient of a helium-storage dewar to vary the sample temperature. This setup

allows one to scan a temperature range from 4.3 K to 295 K (heating and cooling) to measure the variation of resistivity across this range. The rate of cooling/heating in this set-up depends on the speed of sliding, which is controlled by a stepper motor.

The thesis is divided into two parts: the first part discusses the low-temperature resistivity setup (design and measurement protocol along with sample holder and wiring details), and calibration of an uncalibrated Cernox temperature sensor. While the second part focuses on the investigation of intercalated $ZrTe_2$ samples. The chapter in the thesis are organized as follows: The first chapter gives a general introduction to the CDW phenomenon and its relation to SC, which is followed by an introduction to the compound $ZrTe_2$ and a brief review of the previous literature dealing with intercalation studies in this material. The second chapter of this thesis deals with the design and working of the low-temperature resistivity set-up, and temperature sensor (Cernox) calibration detail. In chapter 3, the experimental techniques, including the single crystal growth method, used in this thesis are described. The fourth chapter is dedicated to the crystal growth and structural characterizations of the grown crystal. The resistivity data on the grown and well-characterized crystals is presented in the fifth chapter. Finally, in chapter six of the thesis the thesis has been summarized and conclusions drawn from our investigations are summed up.

1.1 Charge density wave ordering and its origin

A charge density wave (CDW) is a quantum state characterized by a periodic modulation of the electronic charge density in a material, accompanied by corresponding distortions in the atomic lattice [10]. This modulation arises from collective electron behavior, where electrons organize into a spatially repeating pattern due to interactions with the lattice or other electrons. The CDW phase alters the electronic structure of the material, typically opening an energy gap at the fermi surface due to change of translational symmetry (in the simplest case, for example, the doubling of the lattice parameter can occur), which can lead to changes in electrical conductivity and other physical properties. It has been observed that the origin of the CDW and its properties are highly material-dependent. Therefore, the origin of CDW is still under debate.

In the 1930s, Peierls' described the fundamental instability of a one-dimensional (1D) chain (by employing a free electron gas model) with lattice spacing a, demonstrating that an electronic perturbation characterized by the wave vector, $q = 2k_F$ (k_F = fermi vector) can alter the atomic periodicity of the chain to $2a$. This transformation results in the formation of a new unit cell containing two atoms and leads to the opening of an energy gap at the boundary of the Brillouin zone associated with this modified structure (see Figure 1.4). The behavior of the electron gas in response to an external disturbance is characterized by the Lindhard response function $\chi_0(q)$. In one-dimension, the real part of $\chi_0(q)$ exhibits a divergent singularity at $q = 2k_F$ (see the plot

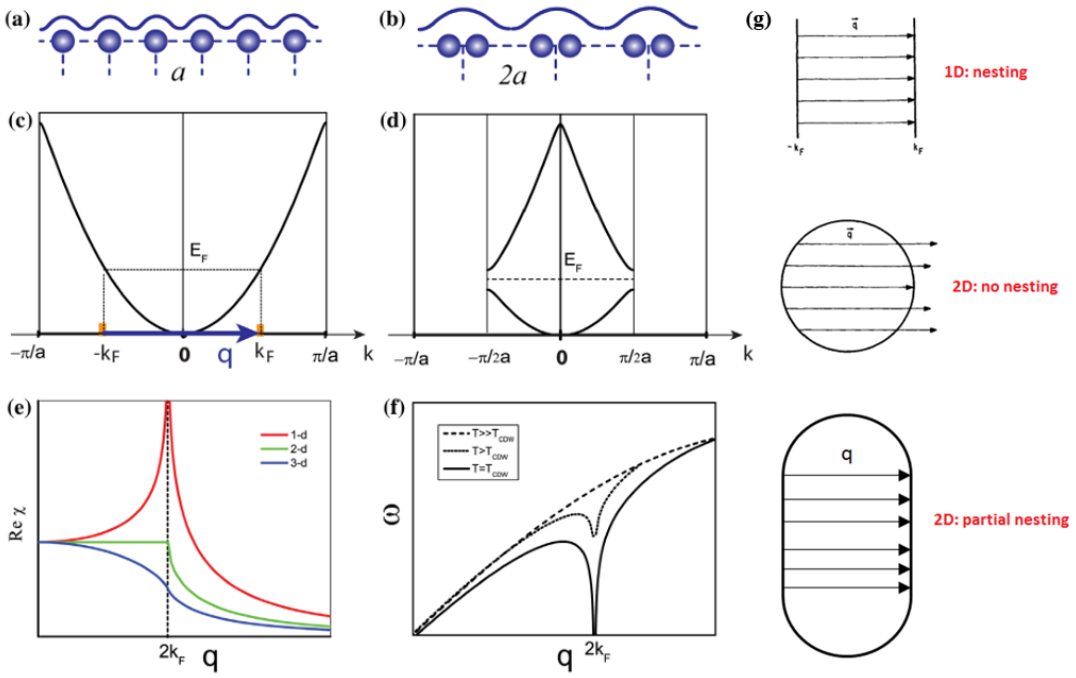

Figure 1.1: Illustration of Peierls' framework; (a) representative image of 1D atomic chain with lattice spacing a; (b) representative image of Peierls' instability leading to $2a$ lattice spacing; (c) electron band dispersion of chain before PLD (d) electron band dispersion of atomic chain for distorted lattice with spacing $2a$; (e) plot of real part of Lindhard's function in case of 1D, 2D and 3D electron gas; (f) variation of phonon energy with temperature (demonstration of Kohn's anomaly); (g) representative image of fermi surface nesting(FSN). Image credit: [37]

of Lindhard's function in (e) Figure 1.4). This divergence signifies that the one-dimensional electron gas is inherently unstable [20]. As a result of the divergence in $\chi_0(q)$, phonon modes with wave numbers near $2k_F$ will experience a renormalization (called as Kohn Anamoly), leading to a reduction in their energy [33] (see (f) in Figure 1.4).

This led to the concept of fermi surface nesting, which is instrumental in explaining the origin of Charge Density Waves (CDW) in higher-dimensional materials. The fermi surface nesting (FSN) refers to the alignment of specific sections of the fermi surface, such that when shifted by a particular wave vector $\mathbf{q}_{CDW}$, the contours overlap ((g) in Figure 1.4 demonstrates the concept of FSN). This overlap leads to a CDW state characterized by the wave vector $\mathbf{q}_{CDW}$ and results in a structural distortion with a periodicity of $2\pi/\mathbf{q}_{CDW}$. Key features associated with CDW in Peierls' framework include fermi surface nesting, the divergence of the Lindhard function, Kohn anomaly, structural transitions, and the metal-to-insulator transition (arising from gap opening at the fermi surface).

However, in higher-dimensional materials, deviations from Peierls' model are often observed; the table in Figure 1.2 from the review article on charge density wave phenomenon [37],

summarizes the characteristics of CDW across various systems (1D, 2D, 3D), and further details regarding the origin of CDW in these contexts are also provided in the aforementioned review article.

	Peierls' model (1D atomic chain)	TTF-TCNQ (Quasi-1D material)	$NbSe_2$ (Quasi-2D material)	Sn/Ge or Pb/Ge (2D films on surface)	Cuprates
Fermi Surface Nesting	√	√ [27]	X [30–32]	√ [37,38]	√ [64,69,70]
Sharp Peak in Lindhard Function	√	√ [23]	X [30–32]	√ [38]	√ [32]
Kohn Anomaly	√	√ [25]	√ [20]	√ [39,40]	X [32]
Structural Transition	√	√ [24]	√ [15–19]	√ [37,38]	√ [67,68]
Metal–insulator Transition	√	√ [22]	X [34]	√ [37]	X [69]

Figure 1.2: Comparison of CDW of various systems with Peierls' Model, credit: [37]

As this work is focuseed on the transition metal dichalcogenides (TMDCs), here we will restrict our discussion to TMDCs. The TMDCs are layered van der Waals materials or 2D materials. Often times, FSN is not observed in 2D materials; in such cases, it is postulated that **q** (momentum) dependent electron-phonon coupling (EPC) drives the CDW transition. For instance in $NbSe_2$ along the Γ–M direction, there is a pronounced peak in g(**q**) (electron-phonon coupling constant) at the wave vector $\mathbf{q}_{CDW}$, which can effectively reduce the energy of the acoustic phonon to zero (as depicted in Figure 1.3), thereby inducing lattice distortion [31]. Strong electron-phonon coupling usually makes phonon energies lower, but it doesn't always cause a significant Kohn anomaly that would lead to changes in the lattice structure.

Here, we briefly discuss the proposed origins of CDW in TMDCs. The pristine 2H-$TaSe_2$ undergoes sequential transitions: an incommensurate CDW (ICDW) at ≈ 122 K and

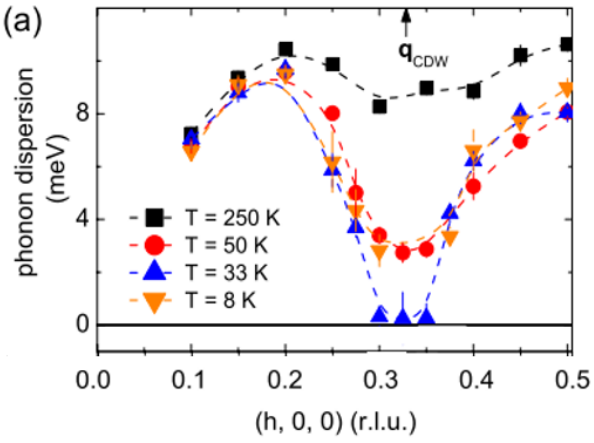

Figure 1.3: Phonon dispersion of 1H-$NbSe_2$ obtained at various temperatures along the (100) direction using inelastic X-ray scattering. Image Credits: [31]

a commensurate CDW (CCDW) at ≈ 90 K. The Proposed driving forces are electron-phonon coupling (EPC) and fermi-surface Nesting. ^{77}Se NMR reveals precursor lattice distortions above T_{CDW}, supporting strong EPC as the driving mechanism [1]. ARPES and optical spectroscopy reveal pseudogaps above the CDW transition temperature ($T_{CDW} \approx 122$ K) and full band gaps in the CCDW phase [28], hinting the role of FSN. However, the q-dependent study of electronic susceptibility shows that electronic instability at the fermi surface alone is insufficient to induce CDW order in 2H-$TaSe_2$ [14]. ARPES studies also indicate the absence of a direct correlation between the fermi surface nesting vectors and $\mathbf{q}_{CDW}$ [14][36], in 2H-$NbSe_2$, 2H-TaS_2 and 2H-$TaSe_2$, questioning fermi surface nesting as the driving mechanism. Moreover, in a few 1T TMDCs($TiSe_2$, TaS_2), electronic correlations are also proposed as driving mechanisms. Therefore, the origins of CDW in TMDCs are highly debated, complicated, and have multiple contributions. To illustrate this point further, Table 1.1 summarises the proposed mechanisms of CDW in $TiSe_2$.

Table 1.1: A list of various proposed mechanisms for CDW in 1T-$TiSe_2$

Mechanism	**Explanation**	**Experimental evidence**	**Ref.**
Excitonic mechanism	Formation of excitons drives a periodic electronic density modulations	ARPES shows temperature-dependent band renormalization; DFT confirms excitonic dominance	[5, 18]
Jahn-Teller (JT) distortion	JT distortion leads to CDW by splitting the Ti-Se bonds into shorter and longer ones	Neutron diffraction data shows a splitting of the Ti-Se bond distances in the CDW state	[12, 32]
Dimensional crossover	Transition from 2D electronic order to 3D structural order stabilizes CDW	ARPES shows distinct orders at 232 K and 205 K; DFT confirms interlayer coupling effects	[18]

It is evident from the discussion above that the characteristics associated with CDW and their origins are highly dependent on the materials, even within the TMDCs. Therefore, any new material added to the list that exhibits CDW offers an opportunity to explore novel aspects of CDW physics.

With this view, we look at the case of $ZrTe_2$. A pristine $ZrTe_2$ sample does not display CDW; however, a recent publication indicates that when a small percentage of nickel is intercalated into $ZrTe_2$, there is a potential coexistence of CDW and superconductivity [6]. The CDW is identified by anomalies in resistivity and specific heat, and a detailed characterization of the superconducting state has been conducted. However, whether CDW is accompanied by a structural transition or not is not yet known. Once this is accomplished, further studies can be undertaken to determine the wave vector $\mathbf{q}_{CDW}$ and explore the potential origins of CDW. Furthermore, the DFT calculations presented in the same article indicate that as the nickel per-

centage increases, the total density of states (TDOS) near the fermi level also rises. When the Ni content reaches 25%, the density of states at the fermi energy increases significantly, creating favorable conditions for spontaneous symmetry-breaking phenomena, such as superconductivity and other electronic instabilities [6]. Similarly, DFT calculations for $Cr_{0.25}ZrTe_2$ show a significant increase in TDOS at the fermi level as well [24].

Moreover, the study of $TiTe_2$ upon intercalation of chromium reveals a charge density wave (CDW) type transition, characterized by anomalies in resistivity and specific heat, as well as the presence of superstructure peaks at low temperatures indicative of a structural transition. Therefore, as part of this work, we investigated Cr_xZrTe_2 (where $x = 0.25 - 0.45$) to examine the effect of intercalation on physical properties and to determine whether any symmetry-breaking phenomena are observed.

1.2 Crystal Structure

1.2.1 $ZrTe_2$

The general formula for TMDC is MX_2, where M is a transition metal and X can be Te, Se, or S. The basic structural unit of layered TMDCs features a transition metal layer positioned between two layers of chalcogen atoms. Within each layer, strong covalent bonds form between the metal and chalcogen atoms. The layers are stacked vertically, with weak van der Waals interactions holding them together. Two widely common phases in TMDCs are 'H' and 'T'. The H-phase forms a trigonal prismatic structure by symmetrically arranging tetrahedrons around the central metal atom. In contrast, the T-phase is an octahedral structure created by rotating one of the tetrahedrons by 180°, typically associated with metallic behavior [11]. The systems under investigation has $ZrTe_2$ as the pristine phase. $ZrTe_2$ exhibits a 1T-octahedral structure with a trigonal symmetry (P-3m1 space group) , as shown in Figure 1.4.

Intercalation in van der Waals materials involves the insertion of atoms, ions, or molecules between weakly bonded layers of two-dimensional (2D) materials as depicted in (d) and (e) of Figure 1.4. Often, intercalation of foreign atoms is used to tune the physical properties of TMDCs. Additionally, the intercalation of atoms also results in the modification of the structure. As part of this study we have investigated Cr intercalated $ZrTe_2$. It is, therefore, essential to discuss the changes in the structure upon intercalation.

1.2.2 $Cr_{0.05-0.3}ZrTe_2$

There are currently no reports of structural solutions obtained for chromium intercalated $ZrTe_2$ from single crystal X-ray diffraction (XRD), which typically provides the most accurate results.

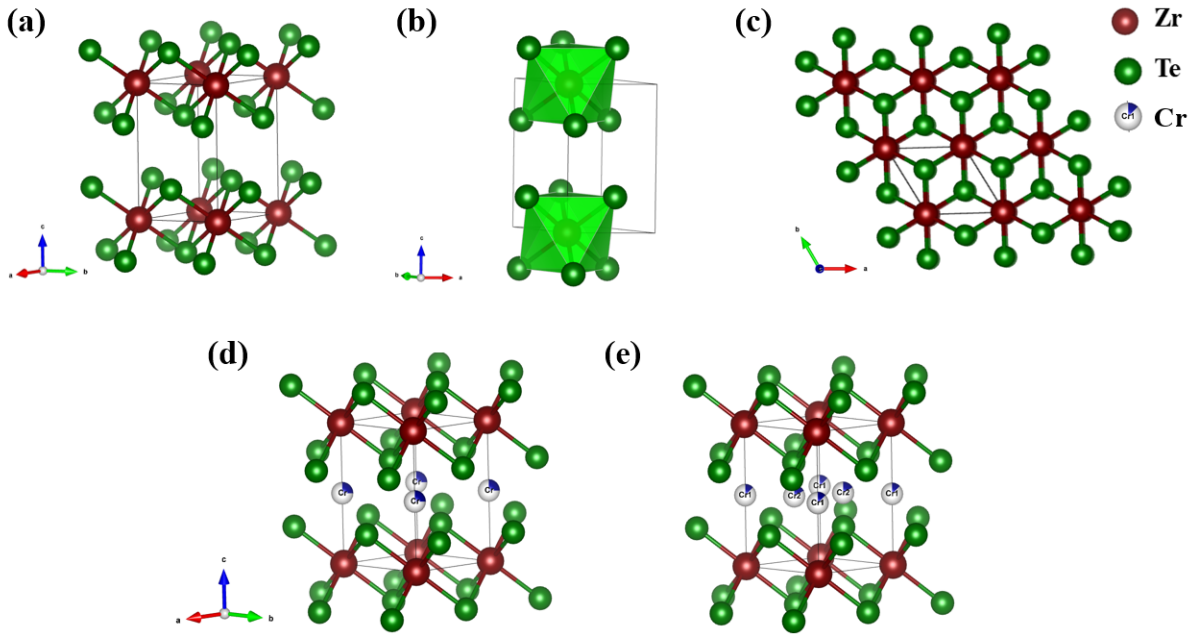

Figure 1.4: Crystal structure of 1T-$ZrTe_2$; a) unit cell of $ZrTe_2$ (brown spheres represent Zr and green spheres represent Te); b) polyhedra formed by the octahedral coordination of Te around Zr; (c) atomic arrangement of a single-layer in 1-T phase (ABC stacking); d) crystal structure of $Cr_{0.25}ZrTe_2$; where chromium occupies only tetrahedral sites (e) crystal structure of $Cr_{0.30}ZrTe_2$; where Chromium occupies both tetrahedral and octahedral sites.

However, a recent study offers a structural solution for Cr_xZrTe_2 (where $x = 0.05-0.30$) obtained through Rietveld refinement using pristine $ZrTe_2$ as a model [24]. Up to $x = 0.1$, all chromium atoms occupy octahedral sites, which leads to a compression of the unit cell, particularly the c-axis. This can be attributed to a compression of the Te-Zr-Te layer due to an effective charge transfer between Zr, Cr, and Te sublattices. As chromium content increases($x \leq 15\%$), about 5% of the Cr atoms start to occupy tetrahedrally coordinated sites in addition to the octahedral sites. At $x = 0.20$, chromium atoms are displaced from octahedral to tetrahedral sites which leads to an expansion of the interlayer spacing. Surprisingly, at $x = 0.25$, all chromium atoms return to occupy only the octahedral sites. This is associated with an ordering phenomenon (suggested further by superlattice peaks in XRD) similar to that observed in other intercalation compounds.

1.3 Magnetic behavior of Cr_xZrTe_2 (M = Zr, Ti)

Chromium intercalation significantly modifies the magnetic properties of the system, the impact of which can be seen in the transport properties (discussed in Chapter 5). We will briefly discuss the magnetic properties of both Cr_xZrTe_2 and Cr_xTiTe_2. Studies on chromium intercalated titanium ditelluride indicate that it exhibits various magnetic states, ranging from a typical paramagnetic state to spin-glass and ferromagnetic states, depending on the intercalant concentration. In certain regions, the spin-glass and ferromagnetic states coexist [2][9][21].

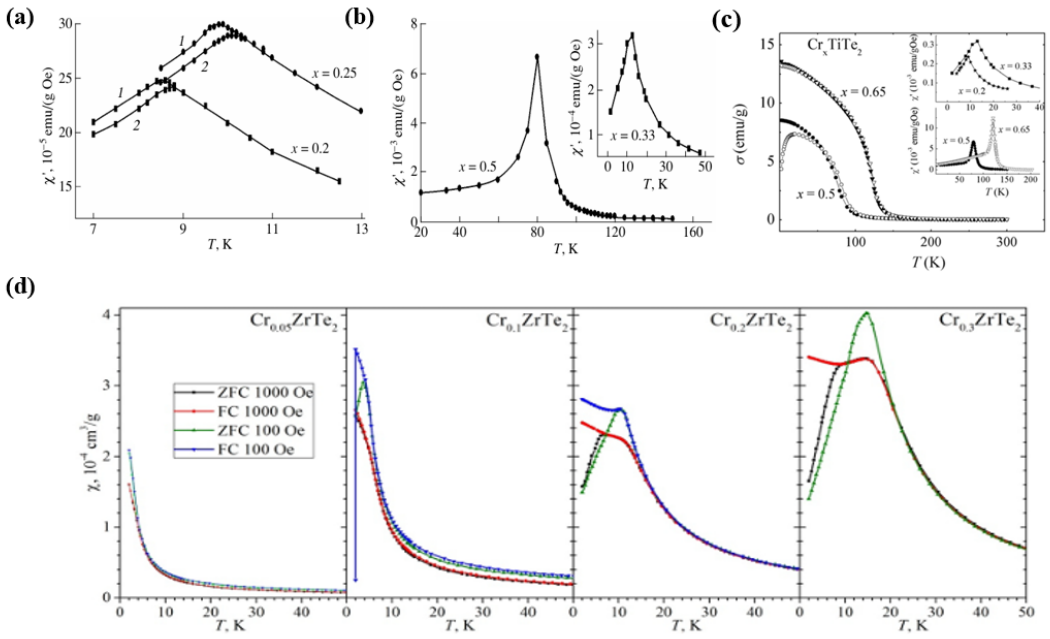

Figure 1.5: Magnetic Susceptibility of Cr_xZrTe_2 and Cr_xTiTe_2. (a) AC susceptibility of Cr_xTiTe_2 ($x = 0.2, 0.25$) at field frequencies of 8 Hz(1) and 800(2) Hz, (b) magnetic susceptibility of $Cr_{0.33}TiTe_2$ and $Cr_{0.50}TiTe_2$, (c) temperature-dependent magnetization plot of $Cr_{0.5}TiTe_2$ and $Cr_{0.65}TiTe_2$. The filled and open symbols represent FC and ZFC data, respectively. The inset displays the real part of the AC susceptibility for Cr_xTiTe_2 at different Cr concentrations, (d) Temperature-dependent magnetic susceptibility plot for Cr_xZrTe_2 ($x = 0.1, 0.2, 0.25, 0.3$) near ordering temperatures in ZFC and FC modes. credits: [2, 24]

The interaction between the magnetic moments of chromium ions is primarily ferromagnetic, as indicated by positive value of Weiss constants obtained from the Curie-Weiss fit, which increases in magnitude with higher chromium content (refer [21]). As illustrated in part (a) of Figure 1.5, for chromium concentrations of $x = 0.2$ and 0.25, the peak in AC susceptibility shifts to higher temperatures as the frequency of the magnetic field increases. This behavior is characteristic of spin-glass systems because it reflects the broad distribution of spin relaxation times in spin-glasses due to their complex energy landscape. Higher frequencies probe shorter relaxation times, requiring higher temperatures to observe the freezing transition. Therefore, the system transitions into a spin-glass state at low temperatures, with freezing temperatures (T_f) of 8 K and 10 K, for $x = 0.2$ and 0.25 respectively. As the chromium content increases ($x = 0.33 and 0.5$), ferromagnetic interactions are enhanced (reflected by large Weiss Constant for these systems). Moreover, field-dependent magnetization measurements at 2 K exhibit hysteresis (refer to [21]). The magnetic moments of chromium ions (as determined by extrapolating the magnetization to zero-field), were found to be 0.2 μ_B for $Cr_{0.33}TiTe_2$ and 0.9 μ_B for $Cr_{0.5}TiTe_2$, notably smaller than the calculated magnetic moment for or a free Cr^{3+} ion (3.87 μ_B), indicating a more complex magnetic behavior. Moreover, neutron diffraction data show relatively small magnetic peaks further indicating that not all Chromium atoms are participating in ordering [21]. The deviation in zero-field cooled (ZFC) and field-cooled (FC) in magnetic susceptibility (see

(c) Figure 1.5) of $Cr_{0.5}TiTe_2$ further confirms the presence of spin-glass behavior. Therefore, in case of $Cr_{0.5}TiTe_2$, the overall magnetic state is proposed to be a combination of both magnetically ordered and spin-glass phases. However, for Cr= 0.65, ZFC and FC overlap (see the susceptibility plot in Figure 1.5(d)), and magnetic hysteresis is also observed, indicating dominant ferromagnetic interactions.

Spin-glass magnetic ordering is observed in Cr_xZrTe_2 for chromium concentrations ranging from x = 0.05 to 0.3. As shown in Figure 1.5 (d), the zero-field-cooled (ZFC) and field-cooled (FC) magnetization measurements diverge. The FC magnetization remains higher than the ZFC magnetization, and the ZFC curve exhibits a sharp drop upon warming, which is characteristic of spin-glass systems. For Cr_xZrTe_2 with x values ranging from 0.05 to 0.3, the temperature at which magnetic ordering takes place decreases as the external magnetic field is increased. It could be attributed to the fact that an increase in the external magnetic field enhances the ferromagnetic component while reducing the antiferromagnetic component. Generally, in intercalated $TiTe_2$ systems chromium atoms occupy octahedral sites but in Cr_xZrTe_2 systems, chromium atoms occupy tetrahedral sites (their minimum distance ranges from 2.508 Å to 2.505 Å), which is smaller than the distance between Cr atoms at octahedral sites. This closer proximity enhances the ferromagnetic interactions, making them comparable to antiferromagnetic contributions. Which could probably explain field-induced magnetic order-disorder transition[24]. The magnetic properties of Cr_xZrTe_2 (x= 0.35-0.45) are not reported yet. However, as part of this work these systems are also investigated.

Chapter 2

Design and working of the low-temperature resistivity setup

2.1 Two Probe vs Four probe methods

As illustrated in the Figure 2.1 (a), in the two-probe resistivity measurement method, the wiring resistances (R_{c1} and R_{c4}) and the contact resistance are also added to the sample resistance value, i.e., the measured resistance value = R_{c1} + R_X + R_{c4}, which can be quite undesirable especially in low-resistivity samples.

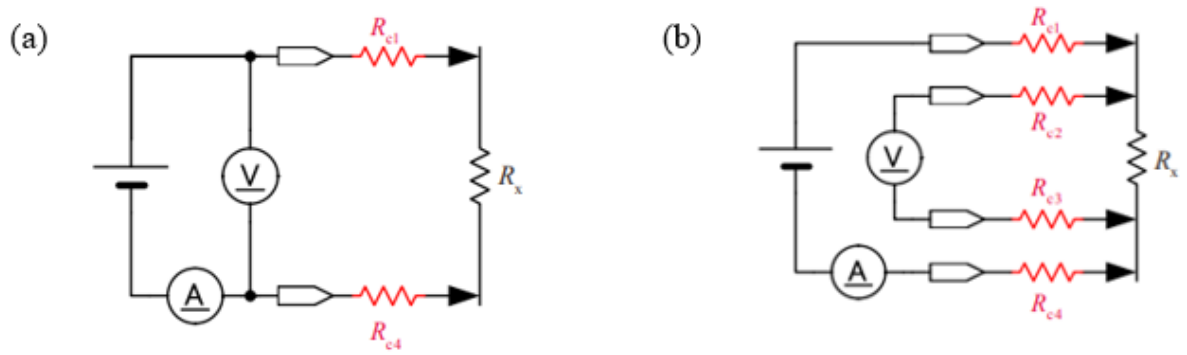

Figure 2.1: schematic of electric circuit for (a) two probe configuration; (b) four probe configuration

However, the four-probe measurement (Figure 2.1(b)) can dramatically reduce the effects of wiring and contact resistance. For most industrial devices, the voltmeter has an input resistance on the order of gigaohms; therefore, the measurement current will not flow through the voltage probes (R_{c1} and R_{c3}). As the voltage drop across R_x is sensed through these voltage probes, it essentially eradicates contact and wiring resistance, significantly increasing the measurement precision for metallic and semimetallic samples. Therefore, the four-probe method is best suited for the purpose of this setup.

2.2 Design of our setup

The setup has a slide-in-type design; a stepper motor lowers or raises the sample chamber into or out of the helium dewar at a controlled speed, which can be made to vary from as small as 5 mm/h to few tens of mm/h. The stepping motor is situated at the base of a threaded spindle, and its shaft is attached to the spindle. The motor rotates the spindle, and the spindle's rotary motion is converted into linear motion, which drives the lever arm connected to the sample chamber (see Figure 2.2). As the chamber descends into the dewar, the temperature of the sample slowly decreases, and the resistivity is simultaneously measured throughout the process. The length of the sample chamber is designed to span the entire length of the storage Dewar, enabling cooling even at low helium levels. A schematic of the entire set-up is shown in Figure 2.2

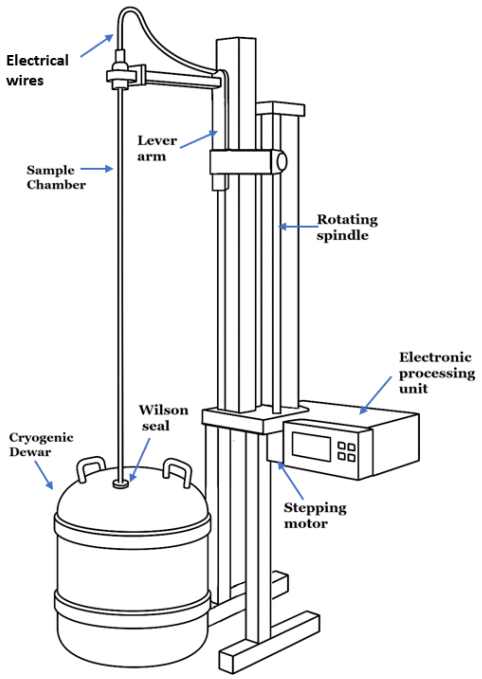

Figure 2.2: A schematic representation of the resistivity setup.

2.2.1 Sample chamber and sample probe

The schematics of the sample chamber and sample probe are shown in Figure 2.3. The sample chamber is 140 cm long and completely made of stainless steel (SS) with an inner diameter of 24 mm and an outer diameter of 28 mm. The sample probe is clamped to the sample chamber via a KF40 flange (c in Figure 2.3) located at the top of the sample chamber. The vacuum ports are located about 10 cm below the SS flange to evacuate or backfill the sample chamber with helium gas ((b) in the schematic).

The sample probe (labeled as II inFigure 2.3) has various components, and each of them is vital to the proper functioning of the setup. It's a top-loading probe clamped to the sample

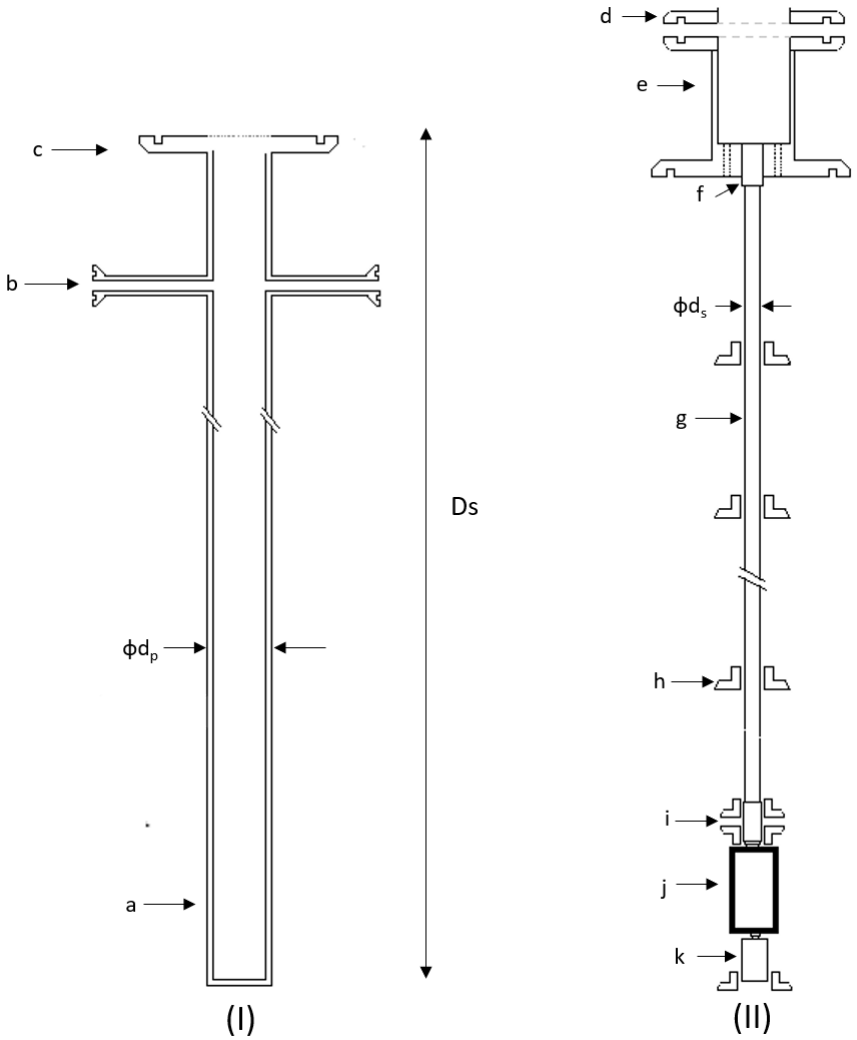

Figure 2.3: A schematic of the resistivity setup used in this thesis. (I) Sample chamber: (a) stainless steel sample chamber; ϕ d_p = 28mm; (b) vacuum ports; (c) clamping plate. (II) Sample probe insert: (d) flange for Amphenol-type electrical feed-through; (e) stainless steel probe holder, which is clamped to the KF-type flange of the sample chamber labeled a; (g) stainless steel tube ϕ d_s = 8 mm; (h) five equally spaced radiation shields; (i) 40 mm long threaded copper heat sink for lead wires; (j) copper frame to keep pin connectors in place; (k) sample holder

chamber using a KF40 vacuum flange (e in the Figure 2.3. At the top of the probe is a 14-pin hermetically sealed Amphenol® electrical feed-through connector (not shown), which is mounted on the Flange d (KF40). A 120 cm long SS tube (g in Figure 2.3 of diameter 8 mm is mounted on the lower side of e (shown as f in Figure 2.3. The SS tube is equipped with five equally spaced radiation shields along the length of the tube, to prevent radiative heating of the sample. These radiation shields are 1.5 mm thick, have a diameter of 17 mm with a small hole for the leads to pass through.

Insulated copper wires (twisted pairs) are wrapped around the entire length of a steel tube, extending up to the Amphenol connector at the top, which is exposed to room temperature and may conduct heat to the sample. To intercept any heat transfer to the sample holder, the

wires are thermally anchored to a copper heat sink located at the lower end of the steel tube (as indicated by 'i' in Figure Figure 2.3). The heat sink is essentially a cylindrical copper block which measures 40 mm in length and has a diameter of 10 mm. The block has disc-shaped collars diameter of 17 mm at its end. A copper frame (labeled j) is screwed at the lower end of the heat sink. The frame is essentially carved out of a copper plate; it's a rectangular frame with inner edges smoothed out, 90.5 mm long. The purpose of this frame is to house the pin connectors (details of the pin connectors are provided in the next section) and keep them in place. The pin-connector is used for mounting and dismounting the sample stage. The lower end of the frame has a threaded screw where the sample stage or holder (labeled k) is attached. At the lowest end a circular stopper is placed to restrict the movement of PCB.

2.2.2 Sample holder

The setup has been designed to measure two samples simultaneously. This requires a sample holder that is large enough for both samples and the Cernox temperature sensor. At the same time, it should be compact enough to prevent the temperature gradients so that the samples and sensor have the same temperature. For this reason, We also need to choose a material that has high thermal conductivity to maintain thermal equilibrium between the samples, temperature sensor, and sample holder. Copper is an excellent choice for the sample holder because it has a specific heat value comparable to brass and stainless steel but possesses significantly higher thermal conductivity. Additionally, to avoid any temperature gradient within the sample holder, the probe is lowered into the helium Dewar very slowly, keeping the sample holder nearly in thermal equilibrium with its surroundings.

The sample holder is cuboid-shaped block fabricated out of high-purity copper metal, with dimensions of 35 mm (length), 10.7 mm (width), and 10.5 mm (thickness). A rectangular groove, measuring 1.9 mm by 2 mm, is cut along the length on the surface of the holder. The dimensions of this groove have been carefully selected to ensure that the three faces of the temperature sensor maintain thermal contact with the sample holder (see (c) in Figure 2.4). This design allows the sensor to be virtually always in thermal equilibrium with the sample holder, optimizing measurement accuracy. The temperature sensor is glued to the sample holder by applying a thin-layer of GE Varnish. A threaded hole of diameter 2 mm is drilled into one of the adjacent faces to securely fasten the PCB for soldering the leads(see (b) in Figure 2.4. To further ensure that the PCB remains in place, a stopper disc is screwed at the opposite end (see (a) in Figure 2.4), which prevents the PCB from turning or rotating about the fastening screw.

We employed 33-gauge insulated copper wires for the electrical leads, configured for a four-probe geometry with four wires (two twisted pairs) for each sample. As shown in Figure 2.4, each lead is soldered to one end of adjacent rows of PCB, arranged in the order of (I^+, V^+, V^-, I^-). To maintain a clear separation between sample 1 and sample 2 leads, one row on the PCB is

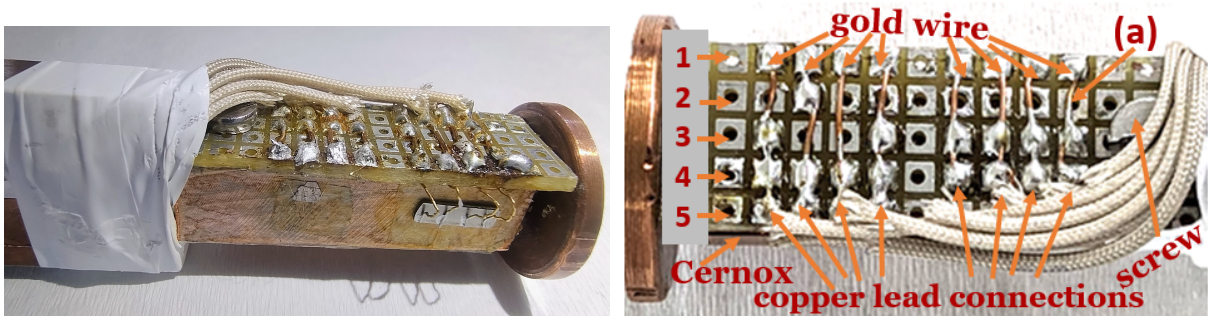

(a) (b)

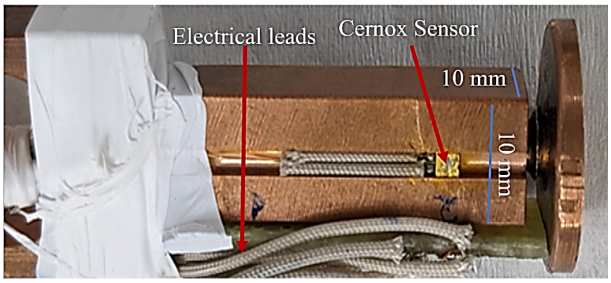

(c)

Figure 2.4: Images of the sample holder (a) a view of the sample holder with sample and PCB on its adjacent faces; (b) a view showing the electrical connections on the PCB; (c) a view showing the placement of the Cernox sensor.

intentionally left blank after placing the leads for sample 1. Each row on the PCB contains five conducting pads along the column. While the copper leads (coming down from the top) are soldered at one end of these rows, at the other end the gold wires are soldered for contacting the sample (see (b) in Figure 2.4). One way to make an electrical connection between two ends of a row is by placing solder over the entire row. Due to their fragility, gold wires often require frequent replacement; however, heating one end to replace the gold wire can cause the solder near the copper leads to melt, disrupting the electrical connection. We used thick copper wires to establish electrical connections between the gold wires and copper leads (see (a) in Figure 2.4 (b)). These wires are soldered to all the conducting pads numbered 1-5 for stability, except for pad 2 (refer to (b) in Figure 2.4). Pad 2 is left unsoldered to minimize heat transfer to the copper leads connection.

On one lengthwise face, PCB is attached, and on one of the adjacent faces, Cernox is attached, and on the other face,the sample is attached. As the sample holder is electrically conducting, a layer of insulating cigarette paper is used for insulation. The sample is mounted using a thin layer of GE varnish. The gold wires are used for making electrical contacts due to their high resistance to corrosion and high electrical conductivity, which is an advantage for measurement on small samples. Four equidistant gold wires are placed on the sample in a line, and conducting silver paste is applied to ensure good elelctrical contacts.

2.3 Electronic components and Circuitory

A 14-pin hermetically sealed Amphenol connector is used. The electrical leads (insulated copper wires) are twisted in pairs(I^+/I^-, V^+/V^-) for noise cancellation due to electromagnetic interference. The leads are covered with fiberglass sleeves around sharp edges, for instance, when passed through radiation shields, to prevent the insulation from scrapping off. The lower ends of the electrical leads are connected to the sockets of two low-temperature PEEK connectors from ICEoxford, UK. The current and voltage leads are confined to separate connectors. The leads are soldered to gold-plated pins on the back of the connectors in a clockwise sequence: sample1, sample2, and Cernox sensor (for example, $I_1{}^+$, $I_1{}^-$, $I_2{}^+$, $I_2{}^-$, $I_T{}^+$, $I_T{}^-$). Voltage leads are also connected in a similar manner. The leads from the plugs are connected to the PCB on the sample holder. The use of PEEK connectors makes the setup more versatile. One of the key benefits is that the sample holder module can be easily removed from the sample probe for sample replacement without impacting other components of the system. This feature is particularly important when dealing with air-sensitive samples, which risk decomposition or oxidation upon exposure to air. PEEK connectors enable users to detach the sample holder from the probe, place contacts within a glove box, and then rapidly reattach and evacuate the setup. This process facilitates resistivity measurements of sensitive samples. Additionally, the design of the sample holder can be readily modified without affecting other components of the setup.

The connections from the Amphenol connector are fed into a KEITHLEY switch system (7001), which operates using an automatic break-before-make switching mechanism. The switch system facilitates simultaneous measurement of multiple samples by switching connections from the electrical leads of one sample to other. It comprises two matrix cards: the voltage leads are connected to card 1, while card 2 has connections to the current leads. The output from card 2 (current card) is connected to a KEITHLEY AC and DC current source (6221), which provides excitation current. Meanwhile, the output from card 1 (voltage card) is connected to the KEITHLEY Nanovoltmeter (2182A) to sense voltage. These three instruments are further connected to a desktop computer via a GPIB (General Purpose Interface Bus) IEEE-488 port and a KEITHLEY® KUSB-488B connector. Shielded cables in twisted pairs and star grounding connections are employed to eliminate noise and avoid ground loops.

2.4 Measurement Protocol and LabVIEW Program

The system is fully automated except for the stepper motor to lower and raise the sample probe in a helium Dewar, whose values should be set manually at the beginning of the experiment. The resistivity acquisition is done using a LabVIEW program developed during the thesis. The measurements are performed in DC mode; the current source provides a constant excitation current to the sample, and voltage is sensed by the nanovoltmeter.

For temperature sensing a Cernox sensor is used. Cernox is a resistance-based temperature detector. We measure the resistance of the sensor and feed it into a calibration polynomial to obtain the temperature (see section 2.5 for more details). To minimize deviation in temperature readings, we measure the resistance of one sample before measuring the Cernox and the resistance of the other sample after that. Since the temperature varies slowly over time, the temperature during measurements for both samples closely aligns with that of the Cernox. The algorithm for a typical measurement is illustrated in Figure 2.5. The current value for each sample is provided as an input before beginning the measurement, as it is a crucial parameter. For instance, high current values can lead to joule heating of the samples, whereas very low current values can result in data noise caused by small voltage readings, particularly in conducting samples.

The switch system is used to send current through only one sample at a time. Once the current is turned on, we wait a few seconds for it to stabilize before starting to take measurements. For each measurement, multiple voltage readings are obtained and averaged to determine v_+ (see Figure 2.5). To eradicate contributions from thermo-electric effects, the polarity of the current is reversed; again, we wait for a few seconds for the current to stabilize and take multiple voltage readings to calculate v_-. Hence, resistance is recorded as mentioned in step 5 of Figure 2.5

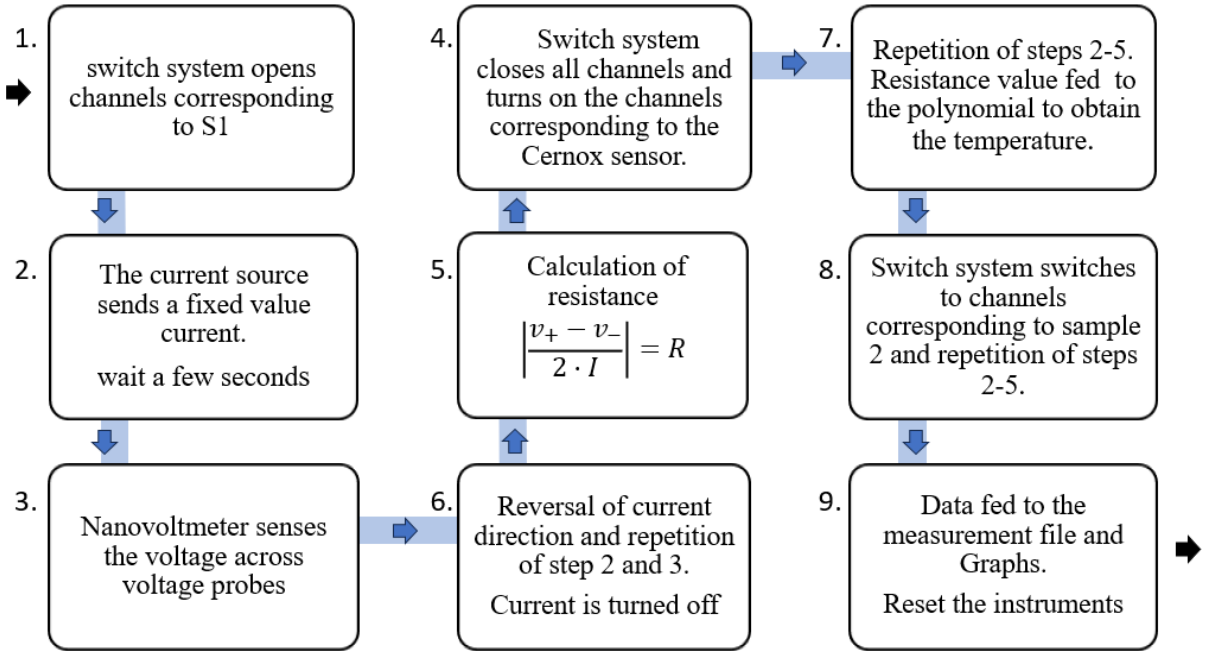

Figure 2.5: Flowchart of LabVIEW algorithm for the measurement of resistivity

The current through the Cernox sensor must be maintained to obtain a voltage drop between 1 mV and 3 mV across the sensor. This ensures compliance with calibration conditions and prevents excessive self-heating. Within the temperature range of 4 K to 298 K, the resistance

of the Cernox changes by nearly two orders, necessitating careful control of the current sent to the sensor to keep the voltage within the specified range. The program has incorporated this control mechanism by utilizing a case structure. The resistance value from the previous while loop serves as input for the case structure that provides a specific current for a defined range of sensor resistance.

2.5 Calibration of Cernox sensor

The Cernox sensor used in the setup was calibrated using a factory calibrated Lakeshore 1050 Cernox sensor. To measure temperature with the Cernox sensor, one must measure its resistance and input this value into a polynomial to obtain the temperature. Detailed information about the calibrated sensor, including resistance values and fitting polynomials, was provided. We calibrated our sensor by measuring its resistance as a function of temperature; using the calibrated sensor for temperature measurement. As a result, we obtained a resistance versus temperature curve in the range of 4.3 K to 296 K, which was then used for polynomial fitting. The class of polynomials used for fitting is Chebyshev polynomials. The specific polynomial used is the following:

$$Z = \log(\text{resistance}) \tag{2.1}$$

$$k = \frac{(Z - ZL) - (ZU - Z)}{(ZU - ZL)}, \tag{2.2}$$

$$\text{T (K)} = \sum_{i=0}^{n} A_i \cdot \cos(i \cdot \arccos(k)), \tag{2.3}$$

Here, ZL and ZU are the lower and upper limits of log(resistance) used in computing Chebyshev coefficients, A_i, the coefficient of (i+1) term in the polynomial. To achieve a better fit, the data is divided into three ranges based on the qualitative changes in the resistivity curve. For example, the slope of the curve becomes significantly steeper as the temperature drops below 80 K, and it is visibly steeper again below 15 K. Therefore, the three temperature ranges selected are 4.3 – 14 K, 14 – 80 K, and 80 – 296 K.

For each temperature range, the data is fitted using equation 2.3 with n being selected between 6 (**6 or 1??**) and 9 by hit and trial so that the resulting polynomials are the best fit. The uncertainty in fit of the polynomial will lead to uncertainty in temperature measurement. The standard deviation of the fit can be calculated using the equation 2.4

$$\sigma_{\text{fit}}^2 = \frac{\sum_{i=1}^{N} (T_i - T_{\text{calc}})^2}{N - n} = \frac{N}{N - n} (\Delta T_{\text{RMS}})^2 \tag{2.4}$$

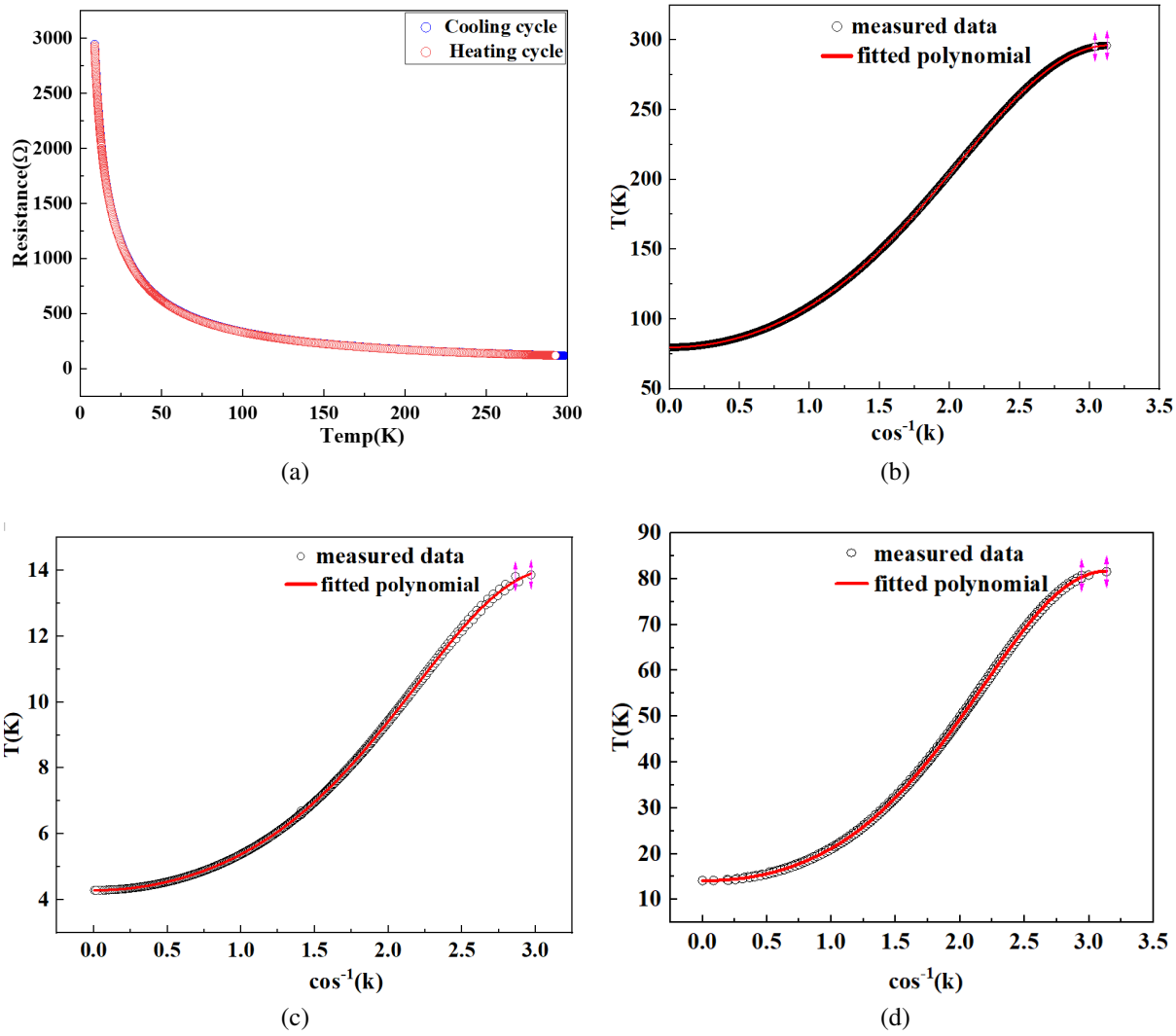

Figure 2.6: Fitting of chebyshev polynomials into R vs T of Cernox, (a) Plot of R vs T Cernox, T (4.3K - 296K); Plot of T vs arccos(k) (b) in temperature range 80 K - 296 K; (C) in temperature range 14 K - 80 K; (d) in temperature range 4.3 K - 14 K

where T_i is the measured temperature for point i, T_{calc} is the temperature obtained from the polynomial for point i, N is the total number of data points, n is the number of fitting parameters, σ_{fit} is the standard deviation or standard error.

For a Gaussian distribution, $2\times\sigma_{fit}$ provides a 95% confidence level, which is used to express the uncertainty in the temperature obtained by the polynomial fitting.Using the same method we obtain uncertainty in temperature obtained from fitting.

$$T\in [80-296]\ K,\ \Delta\ T = 442\ mK,$$
$$T \in [14-80]\ K,\ \Delta\ T = 181\ mK,$$
$$T \in [4-14]\ K,\ \Delta\ T = 50\ mK$$

Table 2.1: Values of fitting parameters corresponding to each temperature range

Cebyshev Eq.	$A_0 + A_1 \cos x + A_2 \cos 2x + A_3 \cos 3x$ $+A_4 \cos 4x + A_5 \cos 5x + A_6 \cos 6x$ $+A_7 \cos 7x + A_8 \cos 8x + A_9 \cos 9x$		
Temperature range	4.3 – 14 K	14 – 80 K	80 – 296 K
A_0	8.20434 ± 0.0019	41.03188 ± 0.02322	171.68437 ± 0.00287
A_1	-4.74381 ± 0.00359	-32.99971 ± 0.03961	-106.43802 ± 0.00608
A_2	0.95319 ± 0.00337	6.78872 ± 0.03747	15.98209 ± 0.00644
A_3	-0.14256 ± 0.00327	-0.85825 ± 0.03648	-1.73672 ± 0.00663
A_4	0.0198 ± 0.0034	0.09964 ± 0.03509	0.17925 ± 0.00662
A_5	0.00306 ± 0.00291	0.03398 ± 0.03446	-0.02253 ± 0.00665
A_6	-0.00437 ± 0.00266	-	0.02241 ± 0.00671
A_7	0.00361 ± 0.00256	-	-0.02086 ± 0.00674
A_8	-	-	0.0135 ± 0.00667
A_9	-	-	-0.00579 ± 0.0067
Reduced Chi-Sqr	6.34612×10^{-4}	0.032739	0.03735
Adj. R-Square	0.99988	0.99978	0.99999

2.6 Validation of the setup

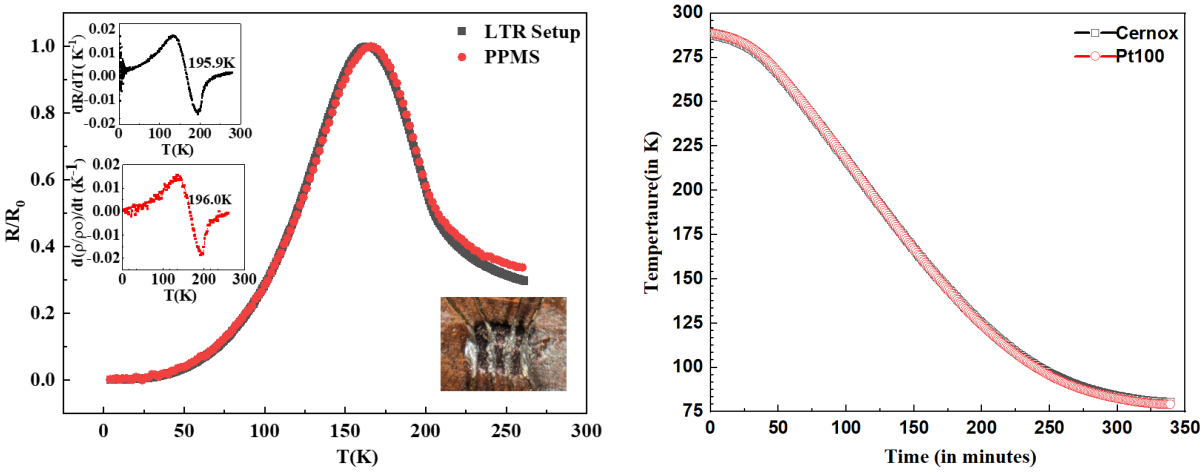

(a) (b)

Figure 2.7: (a) Comparison of PPMS (red) and homebuilt setups (black) data for a $TiSe_2$ crystal grown in our lab; (b) Comparison of measured temperatures at the sample location (Pt100 in the plot) and at the point where Cernox sensor is located.

Commercially available, lead granules (alfa-caesar 99.9%), Niobium chips (sigma Aldrich 99.9%), and a $TiSe_2$ crystal grown in our lab and previously measured with Quantum Design, PPMS. $TiSe_2$ is a van der Waals material, which undergoes a CDW transition near 200 K, which

is manifested as a broad hump in the ρ versus T data. We first measured $TiSe_2$ crystal. To exclude geometric factors, normalized resistance is plotted in (a) Figure 2.7. The transition temperatures obtained by finding minima in dρ/dT from the data of our setup and PPMS data are in excellent agreement. The plots overlap at all temperatures below 225 K; however, a slight deviation is observed at higher temperatures. To check if the thermal equilibrium is maintained between the temperature sensor and the sample, the sample was replaced by a Pt-100 sensor, and the temperature was measured using both the Cernox and the Pt-100 sensors.

Figure 2.7(b) displays the plot of time-dependent temperature variation as measured by the Cernox and Pt-100. An excellent overlap can be seen between the two curves. Small deviations of ≤ 0.5 K above 200 K can be attributed to the low sensitivity of the Cernox at higher temperatures. To validate the setup at low temperatures, we used elemental superconductors: lead and niobium. Lead has a superconducting transition temperature (T_C) of 7.20 K [19], while niobium has a T_C of 9.25 K [30]. Our setup yielded a T_C (T_C is the temperature at which resistivity drops to zero) of 7.20 K for lead, which in excellent agreement with the expected value. For niobium, we observed T_C values of 9.22 K which is also in good agreement with literature value . Moreover, the reported resistivity value of lead at 80 K is 4.9 $\mu\Omega$-cm and that from the data measured using our setup is 6 $\mu\Omega$-cm, demonstrating an excellent agreement. Similarly, the resistivity value of Niobium at 77 K is 2.5 $\mu\Omega$-cm and from our data is 2.9 $\mu\Omega$-cm. Therefore, in both cases, the measured resistivity values are in excellent agreement with the values reported in previous literature.

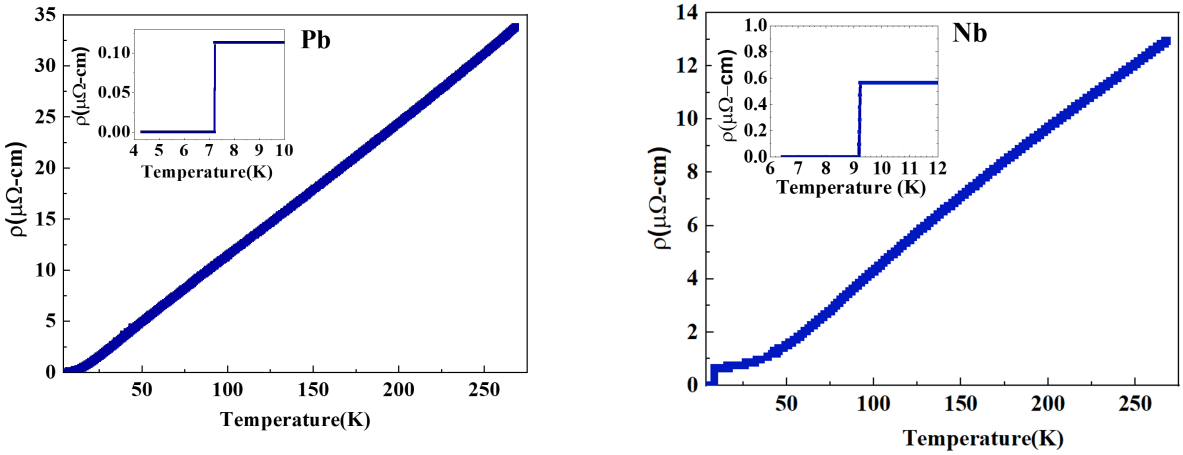

(a) (b)

Figure 2.8: Temperature-dependent variation of resistivity of (a) Lead and (b) Niobium

The step-like behavior observed at low temperatures results from small variations in the resistivity of the samples that could not be captured effectively.

Chapter 3

Experimental Techniques

3.1 Solid-state synthesis

The solid-state synthesis technique is commonly employed to prepare polycrystalline TMDs samples. It requires meticulously combining solid precursors in precise proportions, followed by a series of thermal processing steps.

The synthesis process commences with the precise weighing and thorough blending of precursor materials to ensure uniform distribution. The resulting mixture is then heated to a specific temperature to initiate chemical reactions and form intermediate compounds.

In the subsequent step(s), the powder is often densified by compressing it in the form of a pellet using a uniaxial press. This enhances the density or packing of material and thus facilitates diffusion during the sintering process, leading to the formation of the correct phase. If required, this process is repeated several times either at the same or elevated temperatures to ensure homogeneity and phase purity of the synthesized sample.
The thermal treatment described above enables the diffusion of atoms and promotes chemical reactions, ultimately yielding the desired phase with the targeted crystal structure and density.

The temperature and duration of the sintering process are critical factors and needs to be optimized to achieve the desired outcomes. In some instances, an additional annealing step may be necessary to enhance the material's crystallinity, alleviate internal stresses and achieve intercalation (in case of intercalated samples).

In this project, solid-state synthesis is used to make the intermediate phase for growing crystals using Isothermal Chemical Vapor Trasnport (ICVT) method , presented in Sec. 3.2.2. Moreover, polycrystalline samples of Cr_xZrTe_2 were also separately synthesized using solid-state synthesis.

3.2 Chemical vapour transport

3.2.1 Traditional CVT

Chemical vapor transport is commonly used to grow crystals of TMDCs. This technique is based on a heterogeneous reaction that employs solid-gas equilibria to achieve controlled crystal growth. To perform crystal growth by CVT, the reactants (in their condensed phase) and a transporting agent (for example, iodine) are sealed within a quartz ampoule. The two ends of the ampoule are then heated to different temperatures over an extended period (see Figure 3.1).

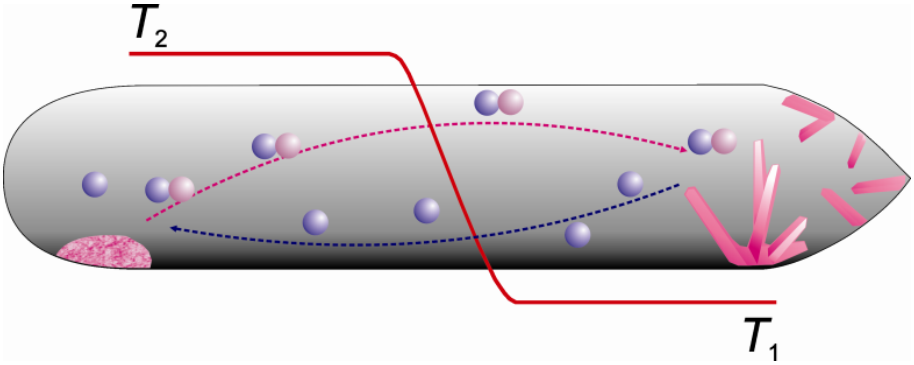

Figure 3.1: Schematic of the traditional CVT process [8]

During the reaction, the condensed phase is volatilized and transported to a different location for deposition. Equation 3.1 illustrates the typical transport equilibrium involved in this process. In this equation, AB_x represents the condensed phase, C denotes the transporting agent, and the right-hand side illustrates the gaseous products formed when the transporting agent interacts with the condensed phase.

$$AB_x\,(s) + nC\,(g) \rightleftharpoons AC_n\,(g) + \frac{x}{y}B_y\,(g) \tag{3.1}$$

The overall growth process can be divided into three essential steps: **forward reaction**, **transport** and **back reaction** (which leads to crystallization). Generally, transport is the rate-determining step in this sequence. To achieve successful crystal growth, it is crucial to optimize the parameters for each step.

Choosing a suitable transporting agent is vital, as it must effectively transfer all components of the condensed phase into the gaseous phase. Additionally, the equilibrium position of the transport reaction should be such that it facilitates the dissolution into the gas phase and the subsequent re-condensation of the solid when experimental conditions change slightly. A suitable temperature gradient is necessary to ensure transport, as $\Delta P \propto \Delta T$. While high temperatures

facilitate diffusion (the transport mechanism). Therefore, optimizing the reaction temperature is also important. The crystal growth is optimized by tuning the above-mentioned parameters.

The crystals of 2D van der Waals materials obtained through CVT are often very thin and fragile, making it challenging to measure their physical properties. As a result, the technique has been modified to enhance the quality, strength, and thickness of the crystals.

3.2.2 Isothermal CVT and Temperature-oscillating CVT

To grow $Ni_{.04}ZrTe_2$ crystals we have employed isothermal CVT (ICVT). In ICVT, pelletized polycrystalline material and iodine are vacuum sealed in a quartz ampoule and heated at constant temperature for extended periods of time. In the absence of a temperature gradient, the gradient of chemical potential between gaseous and solid phase is hypothesized to be the transport mechanism [7].

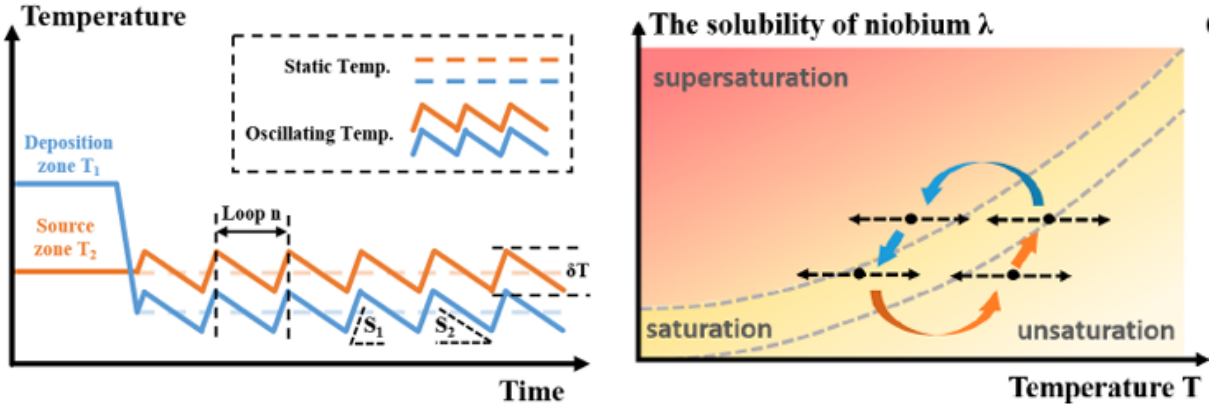

(a) (b)

Figure 3.2: The curve in (a) shows a typical temperature profile, and the diagram in (b) depicts how oscillating temperature CVT utilizes different regions of solubility curve; source zone as unsaturated during warming and supersaturated during cooling, for crystal growth of $NbSe_2$, image credit: [15]

To synthesize Cr_xZrTe_2 crystals, we utilize a temperature-oscillating chemical vapor transport (CVT) method. This technique involves sealing the ampoule similar to that in the traditional CVT. Initially, both ends of the ampoules are heated to fixed temperatures for a brief period. Subsequently, an oscillating temperature profile is implemented (see (a) in Figure 3.2). Both ends of the ampoules are then heated and cooled at the same rate to ensure a constant temperature gradient across the ampoule. During heating, the source zone becomes unsaturated before equilibrium is reached, enhancing the volatilization of the precursor. Whereas during cooling, the deposition zone becomes supersaturated, which promotes the growth of single crystals. This method suppresses screw dislocation-driven growth due to the high degree of supersaturation

during crystallization and improves the physical properties of the crystals [15].

3.3 XRD Technique

Powder X-ray diffraction (PXRD) is a powerful and extensively used analytical technique that allows researchers to determine the crystal structure of crystalline materials. This method involves exposing a powdered sample to an X-ray beam and measuring the pattern of diffracted X-rays produced by the sample using a powder X-ray diffractometer, as shown in Fig. 3.3(a). The diffraction pattern contains valuable information about the arrangement of atoms within the crystal structure, specifically in certain atomic planes.

The fundamental principle behind PXRD is Bragg's law, which states that the diffraction of X-rays by a crystal lattice occurs when the X-rays interact with the planes of atoms in a way that their path difference equals an integer multiple of the wavelength of the X-ray used. This condition can be expressed mathematically as

$$2d \sin\theta = n\lambda$$

, where d is the inter-planar spacing (distance between adjacent crystal planes), θ is the angle of incident X-rays with the plane of the sample, n is the order of diffraction, and λ is the wavelength of the X-ray used (See. Fig. 3.3(b)).

In experimental setups, X-rays are generated from a target material (such as copper, which has a wavelength of 1.5405 Å) through an X-ray tube or generator. Electrons are accelerated towards the target by a high voltage, and when they collide with the target atoms in the anode, X-rays are emitted. The energy of the X-rays produced is determined by the difference in energy levels between the electronic shells involved in the transition, and the X-ray spectrum has characteristic peaks corresponding to different transitions in the target atoms. For example, the K_α and K_β peaks are the most intense in the characteristic spectrum, corresponding to transitions from the L and M shells to the innermost K shell, respectively.

In a typical PXRD experiment, a powdered sample is placed on a sample holder and exposed to a beam of X-rays. The X-rays interact with the atoms in the crystal lattice, producing a pattern of diffracted X-rays that are collected by a detector. The pattern of diffracted X-rays is then analyzed using software programs to determine the crystal structure of the sample.

One of the key advantages of PXRD is that it is a non-destructive technique, meaning that the sample remains intact during analysis. This makes it an ideal method for studying materials that are rare or difficult to synthesize. Additionally, because PXRD is a bulk technique, it can

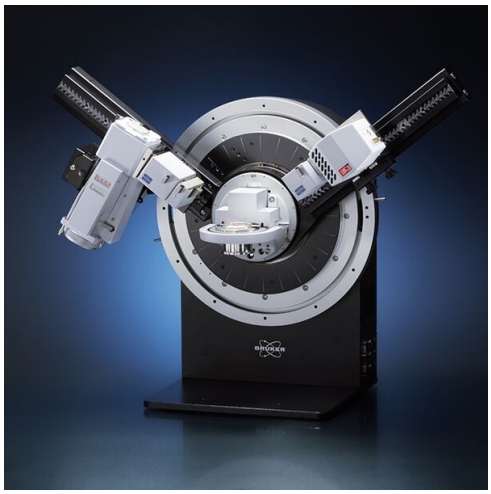

(a)

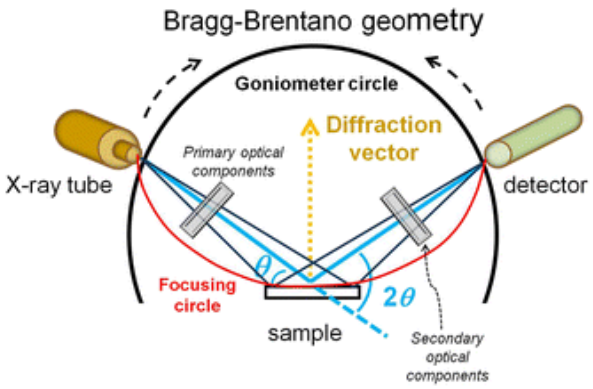

(b)

Figure 3.3: (a) Image of the XRD instrument utilized for conducting PXRD analysis on our samples; (b) A schematic of Bragg- Brentano geometry; Image sources: [22][3]

be used to analyze a large number of samples quickly and efficiently.

For this project, room-temperature Powder X-ray diffraction was conducted using a Bruker D8 Advance diffractometer. The polycrystalline samples were initially ground into a fine powder and then mounted onto a glass slide, whereas single crystal platelets were simply mounted on the slide, exposing the flat facet to the incident X-rays. These prepared samples were then mounted in the diffractometer sample holder. It is important to note that the glass slide is amorphous and does not contribute to the diffraction patterns. The obtained diffraction patterns were then compared to the standard patterns reported in various international crystallographic databases.

3.4 FESEM-EDS

Field Emission Scanning Electron Microscopy (FESEM) is a sophisticated analytical technique used to examine the surface morphology, elemental composition, and dimensions of nanostructures. It employs a Field Emission Gun (FEG) that utilizes a high electric field to extract electrons from a sharp metallic tip, producing a highly focused electron beam. This technique operates similarly to an optical microscope but uses high-energy electrons instead of light and magnetic coils instead of lenses, as shown schematically in Figure 3.4.

FESEM features multiple detectors to capture various emissions and reflections when the electron beam interacts with the sample (see Figure 3.4). Primary electrons are detected by the ASB detector, providing information about the sample's phases. These primary electrons also eject inner-shell electrons, resulting in secondary electrons that are detected by the SE2 and InLens detectors. These detectors are used to study the sample's surface morphology.

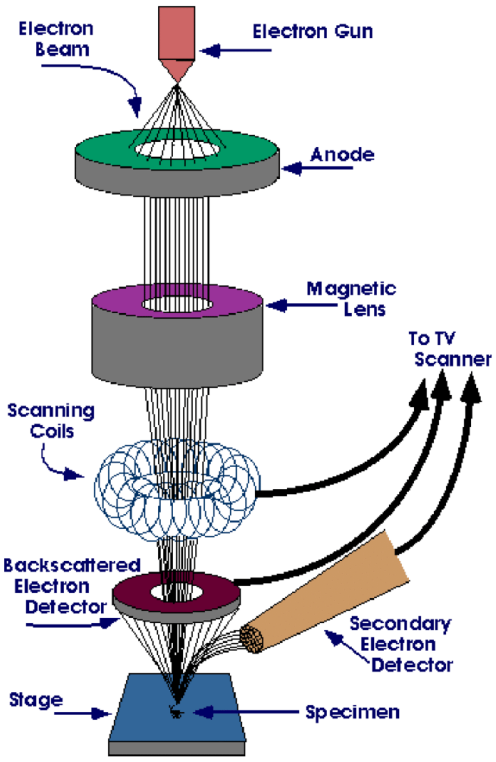

Figure 3.4: A schematic diagram of FESEM illustrating the key components of the device. Image source: [25]

Higher-energy electrons produce characteristic X-rays as electrons transition from higher to lower energy states. These X-rays are detected and converted into electrical signals to form an Energy Dispersive X-ray Spectrometer (EDS), which helps identify the elements present in the sample. However, detecting lighter elements like carbon and oxygen is challenging due to their low-energy X-rays. Energy Dispersive X-ray analysis (EDX) is crucial for quantifying the stoichiometry, or elemental ratio, of components within materials by pinpointing the presence and proportion of elements.

The technical capabilities of SEM-EDX are designed to meet the stringent demands of modern material science. SEM can magnify features up to 50,000 times, revealing subtle details at the boundary level. Concurrently, EDX offers precise stoichiometric analysis down to the submicron level. Together, these techniques provide a comprehensive understanding of the sample's structural and chemical attributes, forming a complete picture essential for materials research and engineering applications. The findings from SEM images and EDX data are instrumental in validating theoretical models and provide foundational insights that guide the development of materials with desired properties and functionalities.

For this thesis, a field emission secondary electron microscope (FESEM) from Zeiss Ultra

Plus, Germany, was used. This setup included an EDS analysis probe with a 20 mm^2 detector from Oxford Inca, offering an energy resolution of 129 eV. The as-grown single crystals were mounted on double-sided carbon tape and placed on the SEM stub. Multiple areas from each sample, as well as several crystals from each batch, were randomly selected for examination of their morphology and composition. The relative atomic percentages of the atoms were used for a quantitative estimation of atomic composition.

3.5 Transport Measurements

The resistivity measurements were carried out in the homebuilt resistivity setup described in chapter 2, which can scan temperatures ranging from approximately 4.3 – 295 K. Some of the resistivity and magnetoresistance were measured in Quantum Design Physical Property Measurement System (PPMS) at the Tata Institute of Fundamental Reserach Mumbai, in the group of Prof, A. Thamizhavel.

To measure high-temperature resistivity, our homebuilt Hall setup is used. The homebuilt high-temperature Hall setup is designed to measure electrical resistivity and Hall effect in samples from room temperature up to 750 K with high precision and temperature stability of ±0.01 K. The key components include a localized heating sample holder, quartz sample chamber, bipolar electromagnets, and lock-in amplifier-based electronic circuitry. The sample holder is made out of stainless-steel with a cartridge heater embedded in it for resistive heating and a Pt-100 sensor for temperature sensing/control using a Cryocon temperature controller. The sample is placed on an aluminum nitride (AlN) base, which has a high thermal conductivity (100 W m^{-1} K^{-1}) for efficient heat transfer but low electrical conductivity to isolate the sample. Ge-Varnish secures the sample on the AlN base. The resistivity was measured in four probe configurations. Contacts were made using silver paint and gold wire, similar to the low-temperature setup.

Chapter 4

Synthesis and structural characterization

As part of this study, we have investigated intercalated $ZrTe_2$. More specifically, we investigated $Ni_{0.04}ZrTe_2$ and Cr_xZrTe_2 samples. In this chapter, the synthesis and structural characterization of these samples is presented in detail.

4.1 Synthesis and structural characterization of $Ni_{0.04}ZrTe_2$

4.1.1 Synthesis

Crystals of Ni-intercalated $ZrTe_2$ are grown using a polycrystalline pellet as a precursor. First, stoichiometric amounts of nickel (Ni), zirconium (Zr), and tellurium (Te) were accurately weighed in the ratio of $0.4 : 1 : 2$ and ground into a fine powder. This powder was then pelletized under a pressure of 3 tons using a KBr cold-press. Following this, the pellet was vacuum sealed in a quartz tube and heated for two days at 950°C and subsequently quenched in ice water. The product obtained was ground again for 30 minutes, pelletized, vacuum sealed, and then heated at 1000°C for 48 hours and quenched in ice water afterward. The resulting pellet was ground a thrid time and pelletized into a 8 mm diameter pellet as before. The obtained pellet was then flame-sealed in an evacuated quartz ampoule (approximately 1 cm radius and 15 cm height) with 150 mg of iodine to perform ICVT(see subsection 3.2.2 for more details). The sealed ampoule was placed horizontally in a box furnace (such that the temperature is the same across the length of the ampoule and conditions for ICVT are met) and heated to 1000°C at the rate 50°C and maintained at 1000°C for 10 days before quenching in the ice water.

Large crystals, measuring approximately 1-2 cm, were successfully grown from the pellet . However, a black deposition appeared on the surface of the crystals (see inset in (a) of Figure 4.1). Multiple trials were conducted to eliminate this deposition. For instance, we quenched one end of the ampoule first in an attempt to deposit the gaseous phase at the colder end opposite the crystals. Additionally, we varied the growth temperature between 900°C and 1100°C to determine if growth temperature affects the deposition. The growth did not occur at temperatures below 950°C or above 1050°C, and in all instances where growth occurred, the

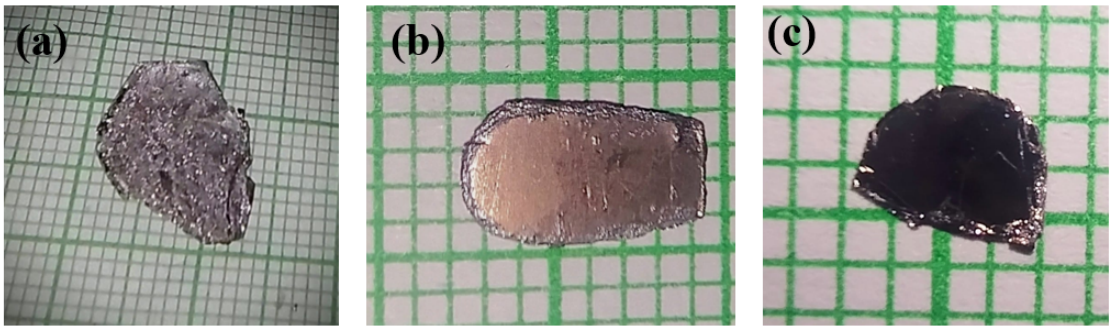

Figure 4.1: (a) Image of the as-grown crystal of $Ni_{0.04}ZrTe_2$, notice the blackish-grey deposition; (b) Image of a polished crystal; (c) Image of the cleaved surface of a $Ni_{0.04}ZrTe_2$ crystal.

crystals exhibited black deposition.

4.1.2 Structural Characterization

The platelet-like crystals were removed from pellet and mounted directly on a glass slide for X-ray diffraction (XRD) analysis. The resulting XRD pattern is shown in Figure 4.2, the peaks marked with asterisks are not associated with any of the Bragg peaks of $ZrTe_2$. The crystals were then polished using 1200 grit sandpaper to eliminate the black deposition from the surface. After polishing, the XRD measurement was repeated on these platelets, revealing only peaks corresponding to the (00l) planes. The intercalation of Ni doesn't give rise to any additional peaks [8]. To gather information about the composition of the black deposition, energy-dispersive spectroscopy (EDS) and SEM images would be necessary. Unfortunately, these analyses could not be conducted due to the limited availability of resources.

To conduct further analysis, the crystals were first polished (see (b) in Figure 4.1) and then cleaved (Figure 4.1 (b) displays a picture of a cleaved crystal) to obtain a clean surface. The PXRD on the platelet of cleaved crystal of $Ni_{0.04}ZrTe_2$ results in (00l) reflections, confirming single crystallinity. As the material is a single crystal, the major contribution to peak broadening is due to microstrains; FWHM of the Bragg peaks is proportional to microstrains; therefore, smaller FWHM implies higher crystallinity [16]. The most intense peak (002) was fitted to a pseudo-voigt lineshape to obtain the FWHM; the obtained FWHM of 0.039°indicates excellent crystallinity. Furthermore, the Laue diffraction pattern of the crystals reveals sharp peaks, indicating excellent crystallinity (refer to Figure 4.3 (a)). The crystals were crushed into a fine powder, and PXRD was performed; the obtained data (panel (c) in the Figure 4.2) doesn't show any extra peaks, further confirming the phase purity of the obtained crystals. However, because the powder is obtained from a crushed single crystal, the (00l) family of peaks have relatively higher intensity due to the preferred orientation.

As has been reported previously the intercalation of Ni doesn't change the XRD pattern

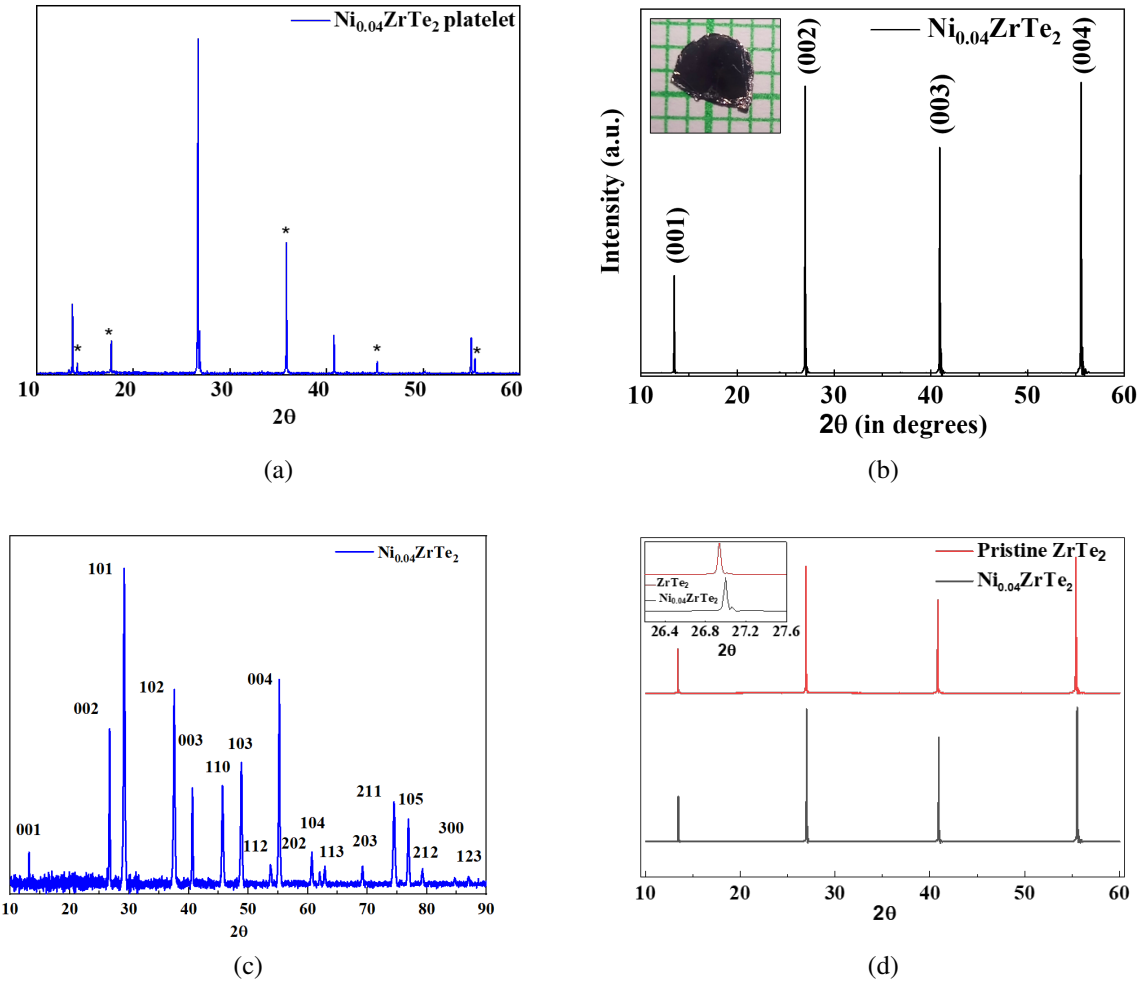

Figure 4.2: XRD data for Ni_xZrTe_2 samples (a) XRD pattern of as grown crystal; (b) XRD pattern of the crystal after polishing; (c) PXRD pattern obtained on powdered crystal of $Ni_{0.04}ZrTe_2$; (d) PXRD patterns of $Ni_{0.04}ZrTe_2$ with $ZrTe_2$ for comparison; inset shows a peak shift to the right upon intercalation of Nickel.

significantly from that of $ZrTe_2$[6]. But Ni intercalation does shrink the c-axis lattice parameter. Figure 4.2 (d) displays the XRD pattern performed on both $ZrTe_2$ platelet as well as $Ni_0.04ZrTe_2$, upon intercalation a shift in Bragg peaks can clearly be observed. However, as the XRD was performed on platelets, displacement due to sample height can also lead to a shift to Bragg peaks. Therefore, we calculated the lattice parameter from XRD data using fitting tools from FullProf, yielding a = 3.9564 $\mathring{A}$ and c = 6.6258 ± 0.0013 $\mathring{A}$, with χ^2 = 9.03. A comparatively large value of χ^2 is due to the preferred orientation in pattern and the large background (comparable to peak intensities) introduced by the sample holder, designed to perform the analysis in an argon atmosphere.

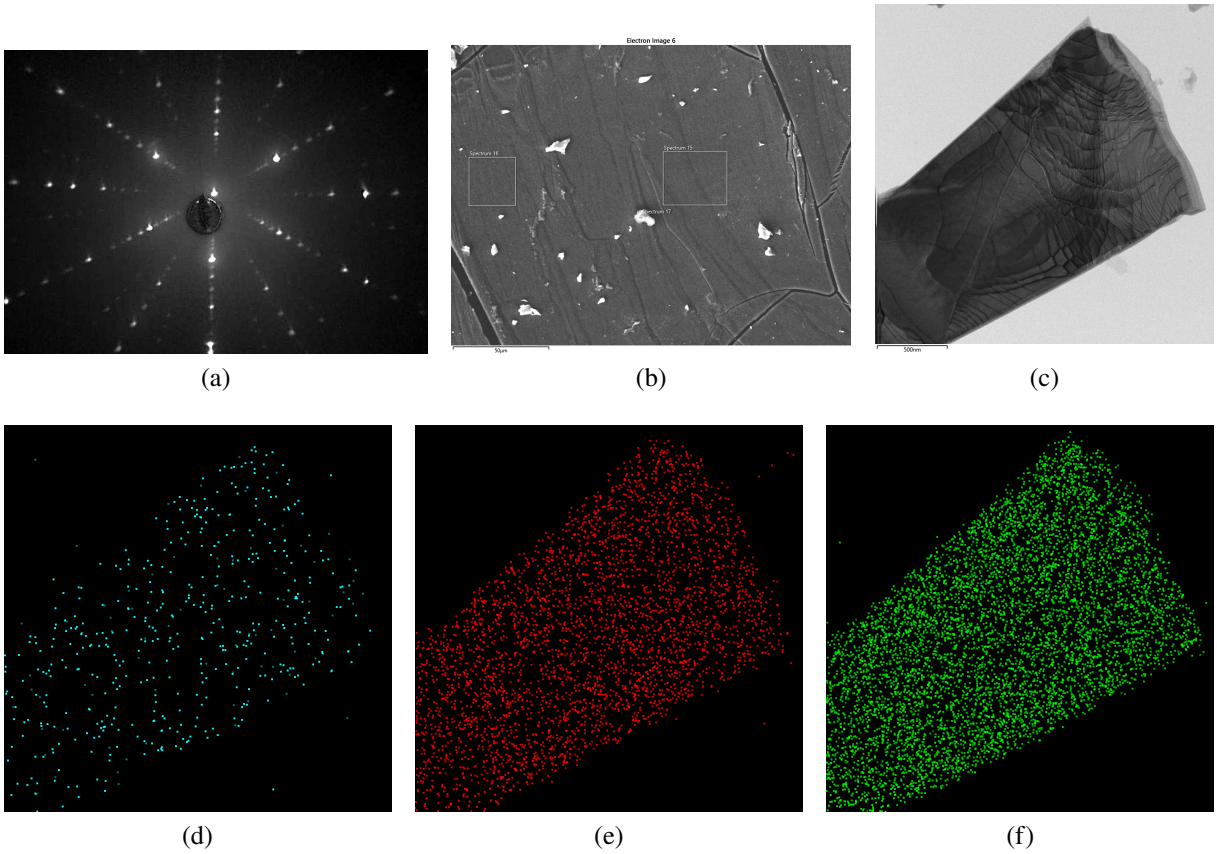

Figure 4.3: (a) Laue diffraction pattern on cleaved $Ni_{0.04}ZrTe_2$ crystal; SEM (b), TEM (c) images of $Ni_{0.04}ZrTe_2$ crystals, (d) Chemical mapping image for Ni $k_{\alpha 1}$; (e) Chemical mapping image for Zr $L_{\alpha 1}$; (f) Chemical mapping image for Te $L_{\alpha 1}$

4.1.3 Elemental mapping and EDS

Scanning Electron Microscopy (SEM) imaging and Electron-Dispersive X-ray Spectroscopy (EDS) analysis were conducted on cleaved crystal samples to eliminate any surface oxidation. The SEM images, as shown in Figure 4.3(a), reveal a uniform composition without any visible secondary phases indicating that the sample is free from impurities. The white particles observed on the surface were identified as glass fragments.

The elemental composition of the samples was determined using EDS, yielding an average stoichiometric ratio of Ni : Zr : Te = 0: 1 : 1.85 ± 0.06. While the ratio of Zirconium (Zr) and Tellurium (Te) is in close agreement with the expected values, Nickel (Ni) was not detected. It is important to note that SEM-EDS has low sensitivity for small doping percentages; in this case, Nickel constitutes only 0.6% by weight . In contrast, Transmission Electron Microscopy (TEM) offers comparatively higher sensitivity. Consequently, chemical mapping and EDS analysis were performed utilizing High-Resolution Transmission Electron Microscopy (HRTEM).

For sample preparation, the crystal was exfoliated using cleaving tape to obtain a thin layer. This layer was subsequently transferred to a polycarbonate, which securely binds to it and placed onto a TEM grid. To facilitate the transfer of the exfoliated crystal, a few drops of chloroform

were applied to dissolve the polycarbonate, resulting in the successful transfer of the crystal onto the grid. The chemical mapping results depicted in Figure 4.3 (c-e) demonstrate a uniform distribution of Ni, Zr, and Te throughout the sample. However, it is important to note that the EDS data obtained from TEM for Zr and Te were unphysical, potentially due to poor calibration of the instrument. Despite this limitation, the chemical mapping data reliably confirmed the presence of Nickel in the crystals.

4.2 Synthesis and structural characterization of Cr_xZrTe_2

While there has been a reported growth of $Cr_{0.40}ZrTe_2$ using chemical vapor transport (CVT) [34], and an X-ray photoelectron spectroscopy (XPS) study has been conducted on $Cr_{0.25}ZrTe_2$ single crystals as mentioned in [24], the details of the temperature profile used during the crystal growth have not been provided. Therefore, to the best of our knowledge, the growth of single crystals for the entire Cr_xZrTe_2 ($x = 0.25 - 0.45$) series has not been reported.

4.2.1 Synthesis and PXRD

The growth of Cr_xZrTe_2 crystals (where x ranges from 0.25 to 0.45) has been conducted using Chemical Vapor Transport (CVT) and temperature-oscillating CVT or OCVT methods. High-purity Zr (99%), Te (99%+), and Cr (99.95%) are mixed in stoichiometric ratios and blended together. The resulting mixture is flame-sealed under vacuum in a quartz tube along with 5 mg/cm^3 of iodine and placed in a two-zone furnace, with the charge positioned at the hotter end. The temperature profile and reaction conditions are meticulously optimized for each x value in order to obtain high-quality single crystals.

To grow the single crystals of $\mathbf{Cr_{0.40}ZrTe_2}$ initially, the protocol reported in [34] was followed, wherein the two ends of the ampoule were slowly heated to 900°C and 800°C for 12 h and kept at this temperature for 7 days, and cooled to room temperature afterward. On the lower temperature end large crystals of length $5 - 15$ mm and $\leq .01$ mm thin were obtained. Two key observations here are that the crystals were very thin and fragile; moreover there was excessive crowding near the tip of the ampoule. PXRD pattern of the platelets showed asymmetric peak broadening (FWHM $\approx 0.047°$) and shift in the peaks indicative of stacking faults and strain in the grown crystals. Generally lower temperatures and smaller temperature gradients are beneficial to reduce thermal defects and excess nucleation. Moreover oscillating temperature CVT also reduces dislocations and increases the thickness of the crystals. Therefore, in a subsequent growth experiment, ΔT was reduced to 80°C, and the two ends of the ampoule were heated to 880°C and 800°C and after maintaining these temperatures for 12 h, both ends were cooled slowly at the rate 0.5°C to 25°C lower and heated back by 12°C/h, and the same cycle is repeated thrice before cooling the ampoule to room temperature. The PXRD pattern on the platelets reveals highly symmetrical and sharp peaks (FWHM $\approx 0.032°$). The XRD pattern and a zoomed-in

view of the (002) peak from the two growth attempts is showm in Figure 4.4.

The same temperature profile is used to obtain high-quality single crystals of the $\mathbf{Cr_{0.35}ZrTe_2}$, confirmed by the PXRD pattern indicating highly symmetrical and sharp peaks (FWHM of most intense peak ≤ 0.035).

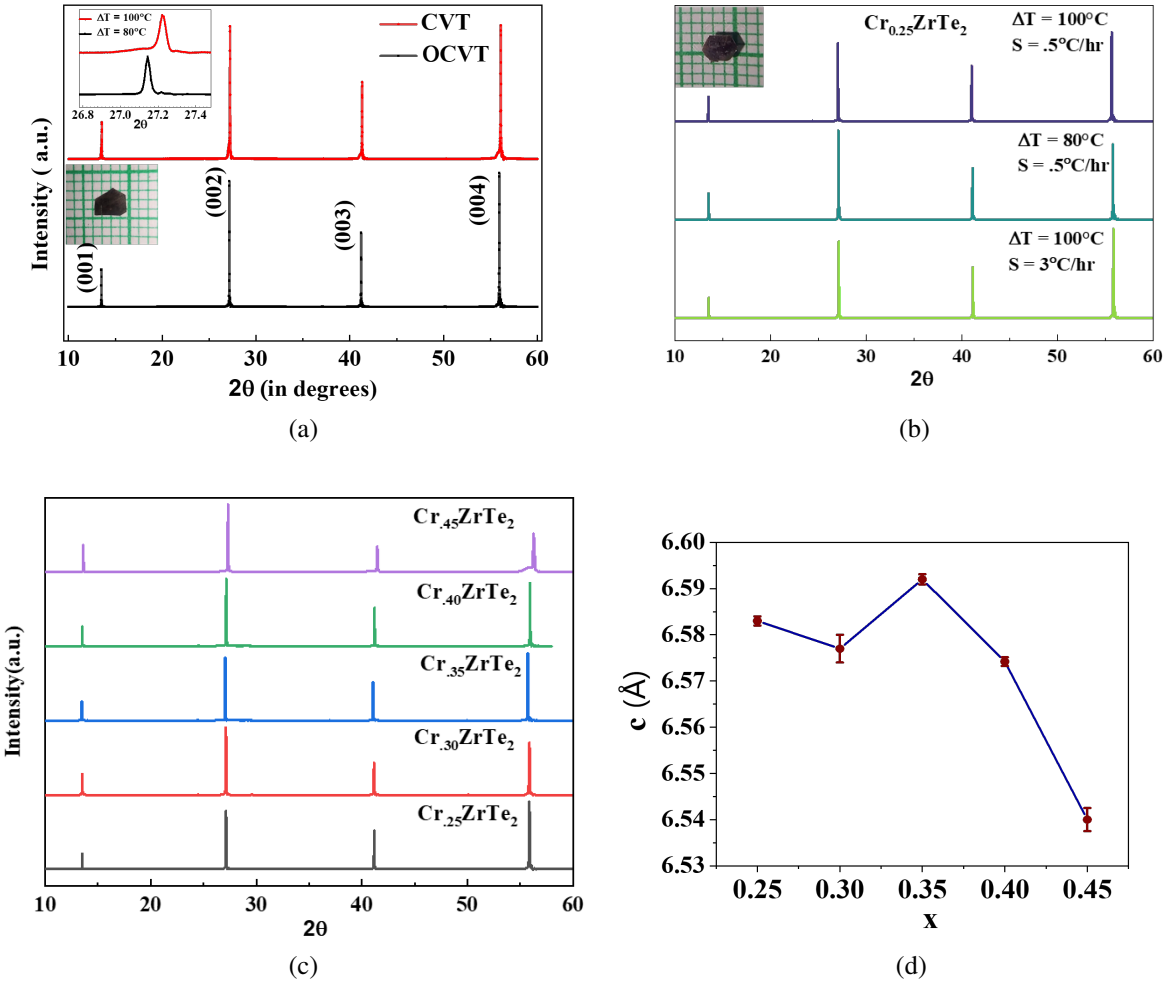

Figure 4.4: XRD analysis of Cr_xZrTe_2 samples; (a) PXRD plots of the $Cr_{0.40}ZrTe_2$crystals grown by maintaining temperature gradient of 100°C (black) and 80°C(red); (b) XRD pattern of $Cr_{0.25}ZrTe_2$ single crystals from various growth conditions; (c) PXRD pattern of Cr_xZrTe_2 single crystals with varying x values; (d) lattice parameter(c) trend with varying x-value

When traditional chemical vapor transport (CVT) is used to grow crystals of $Cr_{0.25}ZrTe_2$ with a temperature difference (ΔT) of 100°C, very small crystallites, measuring less than 1 mm in length, are observed (see Figure 4.5 (c)). Increasing the temperature gradient does not improve the crystallite size, indicating that while transport is occurring, the backward reaction is not favored. As discussed previously, OCVT enhances the backward reaction by increasing the degree of supersaturation. Therefore, in subsequent experiments oscillating CVT is employed for the growth of both $\mathbf{Cr_{0.25}ZrTe_2}$ and $\mathbf{Cr_{0.30}ZrTe_2}$.

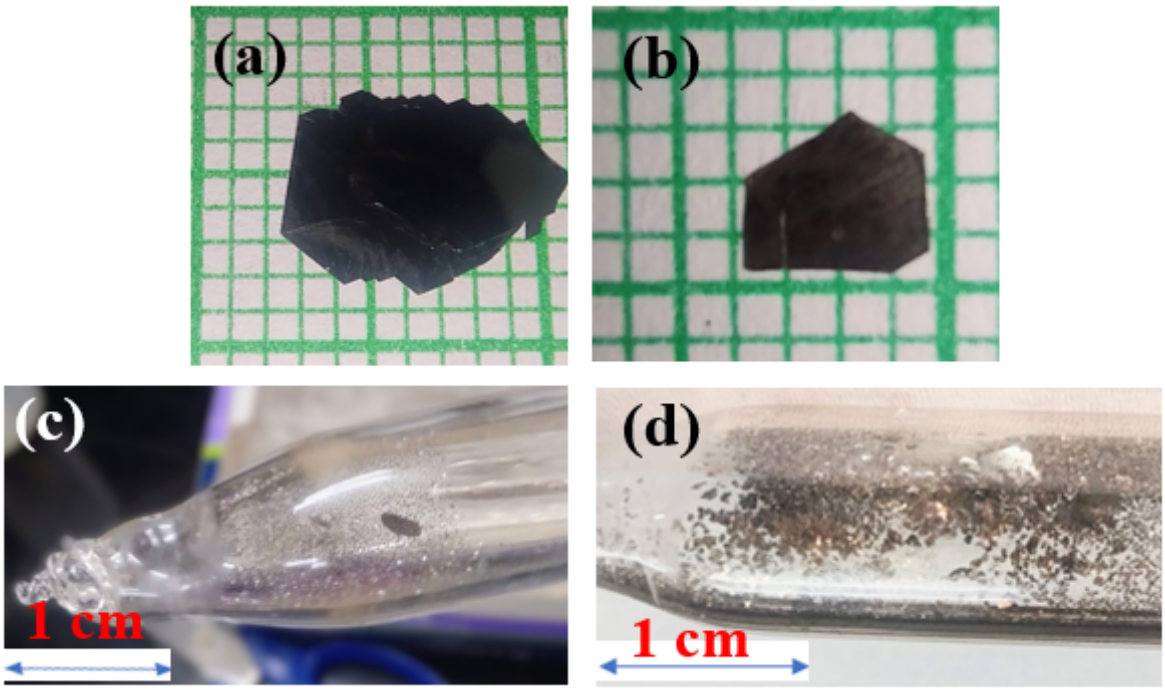

Figure 4.5: (a) Image of a $Cr_{0.45}ZrTe_2$ crystal; (b) Image of a $Cr_{0.40}ZrTe_2$ crystal; (c) micro-sized crystal of $Cr_0.25ZrTe_2$ obtained by traditional CVT; (d) Crystals of $Cr_0.25ZrTe_2$ obtained by temperature oscillating CVT.

A general temperature profile for growth consists of heating one end to 900°C (the source) and the other to 800°C (the sink). After maintaining this temperature for 12 h, both ends were cooled slowly at a rate of S°C/h until they reach 25 degrees lower than the original temperatures. The temperature is then increased back by 12°C/h. This cycle is repeated for seven days, and the system is subsequently cooled to room temperature.

Figure 4.4(b) displays the X-ray diffraction of a crystal of $Cr_{0.25}ZrTe_2$ grown under three slightly different temperature profiles. In the first scenario (C_1), a temperature gradient of 100°C is maintained, with a cooling rate of 3°C/h. In the second scenario (C_2), the cooling rate is reduced to 0.5 ◦C/h, and in the third scenario (C_3), the source zone temperature is lowered to 880°C while the sink temperature remains unchanged, creating a temperature difference of 80°C ($\Delta T = 80°C$) at a cooling rate of 0.5°C/h. However, the FWHM of the most intense peak is less than 0.04° for the crystals obtained in all three cases; C_1, C_2, and C_3. While, the Full Width at Half Maximum (FWHM) of the most intense peak is comparable for both C_1 and C_2, but it is larger for crystals grown in scenario C_3. Additionally, some crystals from C_3 display a shoulder peak at higher 2θ values, which indicates phase inhomogeneity.

The average size of crystals in scenarios C_2 and C_3 is approximately 5 mm, with the largest crystal reaching lengths of up to 1 cm (see inset of Figure 4.4 (b)). The thickness of these crystals varies from 50μm to 200 μm, with smaller crystals exhibiting greater thickness. In contrast, the average size of crystals in C_1 is close to 1 cm, and their thickness is comparable to

that of the other scenarios. Therefore, the growth conditions presented in both C_1 and C_2 yield good quality crystals.

Figure 4.4 (c) dispalys PXRD pattern on Cr_xZrTe_2 platelets, the XRD peaks shifts to right when x increases from 0.35 to 0.45 indicating a compression of the unit cell perpendicular to basal plane, however for x = 0.25 - 0.35, the variation is non-monotonous, which is further reflected in calculated **c** values. As the x value is increased, the compression of the unit cell along c-axis is expected due to the compression of the Te - Zr - Te sandwich, which is attributed to covalent interactions formed between Zirconium atoms and the Chromium atoms, facilitated by Zr $4d_z^2$/Cr $4d_z^2$ hybridization [24]. Generally, in TMDCs, intercalated atoms occupy the octahedral sites, however, in the case of Cr_xZrTe_2 systems, the Chromium atoms tend to occupy tetrahedral sites as well (as discussed in subsection 1.2.2). The presence of intercalant atoms within tetrahedral sites inhibits the development of hybridized states. As a result, when these sites are occupied by intercalated species, lattice compression is not observed; which could be the reason why we observe a slight increase in lattice parameter (**c**) from x = 0.25 - 0.35. However, SXRD analysis is required to confirm the occupation of tetrahedral sites by Chromium atoms for x = 0.30 and 0.35.

4.2.2 EDX and SEM Analysis

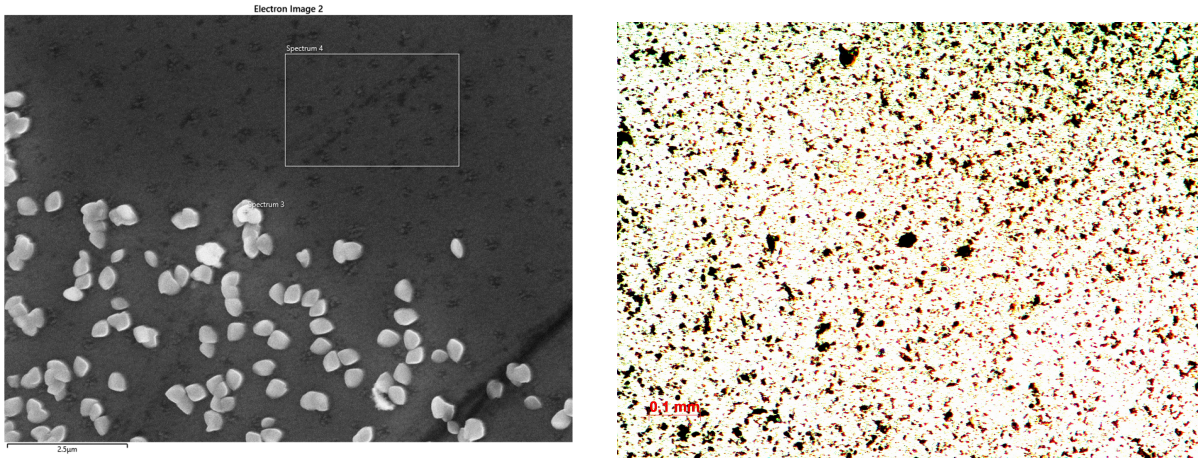

(a) (b)

Figure 4.6: (a) SEM image of $Cr_{0.25}ZrTe_2$ crystal; (b) optical microscopy image of $Cr_{0.25}ZrTe_2$ crystal in 10x magnfication

Scanning Electron Microscopy (SEM) imaging and Electron-Dispersive X-ray Spectroscopy (EDS) analysis were conducted on as-grown crystals at TIFR Mumbai. The crystals were vacuum-sealed in a quartz tube and stabilized with quartz wool to protect them. Therefore, the white particles on the surface of the crystal in the SEM image (Figure 4.6 (b)) were identified as quartz fragments from the wool. The SEM images for a 25% Cr intercalated samples, shown in

Figure 4.6, reveal a contrast between different areas of the sample, which is generally associated with a difference in electron density in the area, suggesting a secondary phase. Figure 4.6 (b) displays an optical microscope image of the 25 % intercalated crystal, and the surface of the crystal shows microsized pores (the black regions in the image) on the surface. Therefore, in our case, the regions with dark contrast are due to the surface morphology of the crystal. To further confirm this, point mapping using EDS was performed in these regions having darker contrast; which was in agreement with the expected composition of our sample. The crystals were vacuum-sealed in a quartz tube and stabilized with quartz wool to protect them. The white particles on the surface were identified as quartz fragments from the wool. The elemental composition of the samples was determined using EDS, yielding an average stoichiometric ratio of Cr: Zr: Te = 0.25: 1: 2.1 ± 0.06, which is in close agreement with the expected composition. To further confirm the variation of composition from crystal to crystal within each batch, eds-sem analysis should be done in future (due to the breakdown of FESEM facility in our institute such measurements could not be done at present).

Chapter 5

Transport Study

The pristine $ZrTe_2$ is suggested to be a semimetal, due to the presence of an equal electron and hole carrier density [26], low thermal conductivity (5.4 W m^{-1} K^{-1})[17], the crossover of valence and conduction band at fermi level [13]. The pristine $ZrTe_2$ exhibits metallic trend in its resistivity [36][29]. However, its low-temperature behavior is highly sensitive to the self-intercalation of zirconium (Zr) between the van der Waals layers. For example, it has been reported that the resistivity drops to zero at 2 K, i.e., the sample becomes superconducting [36][29]. Conversely, another study indicates an increase in resistivity around 8 K, which is attributed to the presence of self-intercalated Zr atoms[29]. As part of this thesis, we have investigated highly intercalated as well as lightly intercalated $ZrTe_2$ systems.

5.1 $Ni_{0.04}ZrTe_2$

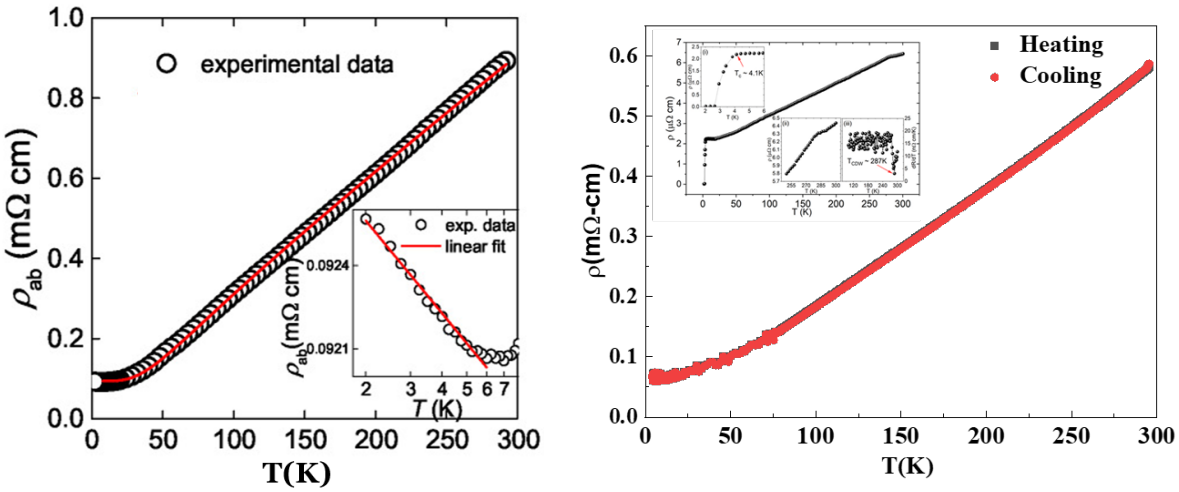

(a) (b)

Figure 5.1: (a) Resistivity behavior of pristine $ZrTe_2$, image credit: [29]; (b) Resistivity behavior of $Ni_{0.04}ZrTe_2$ in the temperature range 4.5 K- 295 K, measured in the homebuilt set-up.

The Figure 5.1 displays the resistivity trend of $Ni_{0.04}ZrTe_2$ crystals that were previously reported to have CDW transition characterized by a small anomaly in resistivity at 287K [6]. As can be seen from the data plotted in this figure, no anomaly was observed in our sample. As discussed previously, the presence of Ni in the system was confirmed using HRTEM chemical mapping data. However, accurate determination of Ni content wasn't possible. The absence of anomaly doesn't necessarily imply the absence of CDW as discussed in [37]. Therefore, we plan to do a STM study on the system to investigate further the presence of CDW, which can be probed utilizing both STM imaging and STM spectroscopy. Moreover, it could be possible that, indeed, no CDW transition is present in our case as the properties of the $ZrTe_2$ are highly sensitive to the presence of self-intercalation of zirconium [29][36].

5.2 $Cr_{0.25}ZrTe_2$

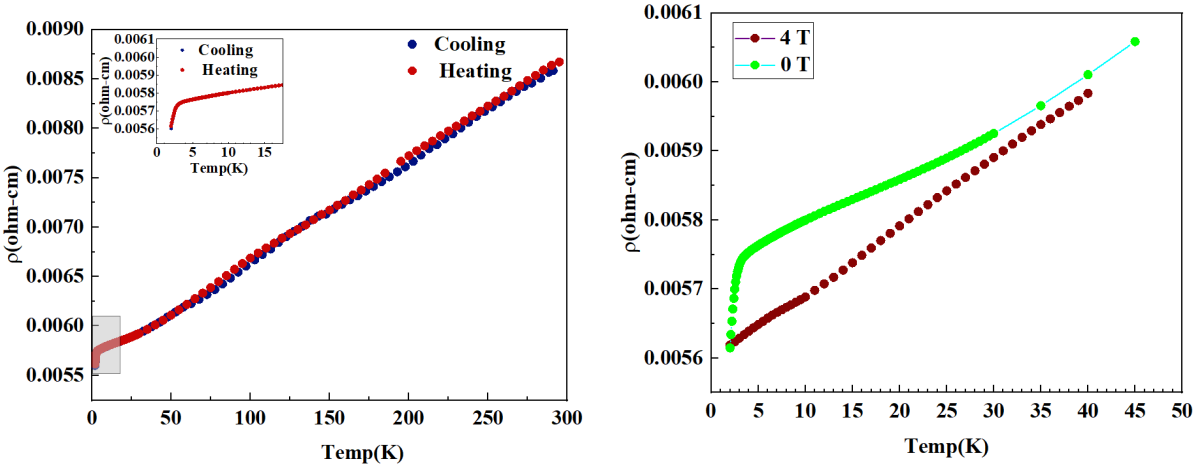

(a) (b)

Figure 5.2: Temperature dependent resistivity plots of $Cr_{0.25}ZrTe_2$; (a) in the absence of magnetic field; (b) resistivity of $Cr_{0.25}ZrTe_2$ in presence of magnetic field (4 T) plotted alongside the zero-field data for comparison

The resistvity of $Cr_{0.25}ZrTe_2$ was measured using the transport option in a PPMS at the Tata Institute of Fundamental Research, Mumbai. In the case of $Cr_{0.25}ZrTe_2$, near 4 K a drop in the resistivity is observed as depicted in Figure 5.2(a). However, the resistance did not go to zero down to the lowest measurement temperature of 2 K. This drop in $\rho(T)$ is likely a superconducting drop as it was previously reported that $Cr_{0.40}ZrTe_2$ undergoes superconducting transition below 5.4 K [15]. And it was previously discussed that at x = 0.25, Cr in Cr_xZrTe_2 gets ordered, suggested by superlattice peaks in PXRD pattern; enhancing density-of-states (DOS) in the vicinity of the fermi energy, which favors symmetry-breaking phenomena like superconductivity [24][6]. To investigate whether the drop in $\rho(T)$ below 4 K is indeed due to the onset of superconductivity, the resistivity was measured in the presence of a magnetic

field. $ZrTe_2$ based samples typically have very small critical magnetic fields, less than 0.5 T [36]; therefore, we expect a high field of 4 T to kill the superconductivity, if present. However, while the resistivity drop indeed disappeared, alongside that we also witnessed a significant negative magnetoresistance (see Figure 5.2 (b)) over a broad temperature range. As discussed in section 1.3, the Cr_xZrTe_2 system exhibits dominant ferromagnetic interactions. Consequently, the negative magnetoresistance can be explained by the field polarization of Cr moments, which leads to a reduced spin-disorder scattering cross-section and, in turn, lowers the resistivity.

The resistivity drop alongside negative magnetoresistance suggests the presence of some ordering phenomenon, which could be filamentary Superconductivity, as the Superconducting transition remains incomplete down to 2K. However, the possibility of the ordering phenomenon being magnetic in nature or the coexistence of superconductivity with a magnetic phase can not be ignored.Therefore, to determine the nature of the ordering phenomenon, magnetic susceptibility, and specific heat measurements are necessary.

5.3 $Cr_{0.40}ZrTe_2$

$Cr_{0.40}ZrTe_2$ sample was also measured using a PPMS at TIFR Mumbai. When chromium content is increased to 40% an upturn in resistivity appears near 16 K as depicted in Figure 5.3 (a). There could be various origins of the upturn observed at low temperatures. For instance when ferromagnetic clusters are present in the system at lower temperatures, Kondo-like spin-flip scattering from the significant localized moments (moment of the cluster) may take place, resulting in a contribution of -ln(T) type, with an increase in resistivity as the temperature decreases at very low temperatures [23]; which is proposed to be the reason for the upturn in resistivity observed for $Cr_{0.25}TiTe_2$ at low temperatures, which vanishes upon application of magnetic field [2]. Moreover, it can also occur from the gap opening. Therefore, to investigate the origin of the upturn in resistivity in our sample, we have fitted the data using various electronic transport models.

The resistivity data in the case of $Cr_{0.40}$ $ZrTe_2$ samples is best explained by a $\sqrt{T}$ dependence (displayed in Figure 5.4(a)), which remains valid down to the lowest measured temperature of 2 K In contrast, the behavior characterized by -ln(T) does not adequately account for the increase in resistivity or only does so within a limited temperature range, showing notable deviations at lower temperatures (see (b) in Figure 5.4). We also applied the Arrhenius model (not shown) and variable range hopping models (depicted in Figure 5.4(c)) to fit the low-temperature resistivity upturn, which were also unsuccessful (results for Arrhenius fit not displayed). Therefore, the analysis of resistivity data strongly supports a $\sqrt{T}$ dependence as a suitable description for the low-temperature resistivity increase compared to other commonly used functional forms, which indicates that at lower temperatures, inelastic electron-electron interactions (EEI) arising from repeated impurity scattering may be responsible for the observed rise in resistivity below 15 K.

It was suggested in [24] that ferromagnetic interactions are significantly enhanced in Cr_xZrTe_2 systems due to the occupation of tetrahedral sites by chromium atoms, which reduces the distance between chromium ions. Consequently, the deviation from Kondo behavior can be attributed to the presence of strong ferromagnetic interactions, leading to the formation of large clusters in $Cr_{0.40}ZrTe_2$, surpassing the Kondo limit.

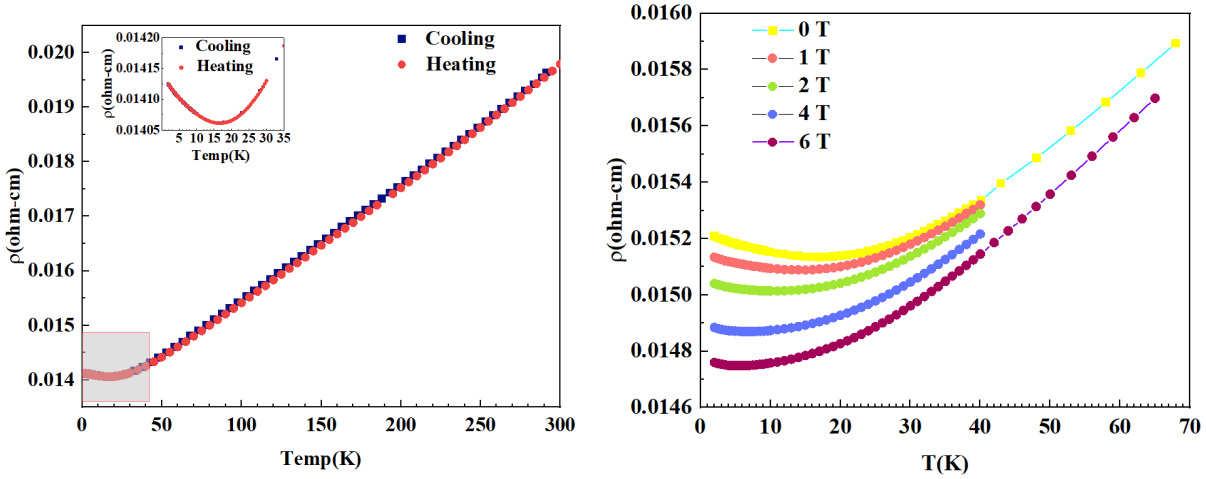

(a) (b)

Figure 5.3: (a) Temperature-dependent resistivity of $Cr_{0.40}ZrTe_2$ in the absence of magnetic field; (b) Resistivity $Cr_{0.40}ZrTe_2$ at low temperatures in the presence of magnetic field 1 T (orange), 2 T (green), 4 T (blue), 6 T (brown). The zero-field data (yellow) is shown for comparison.

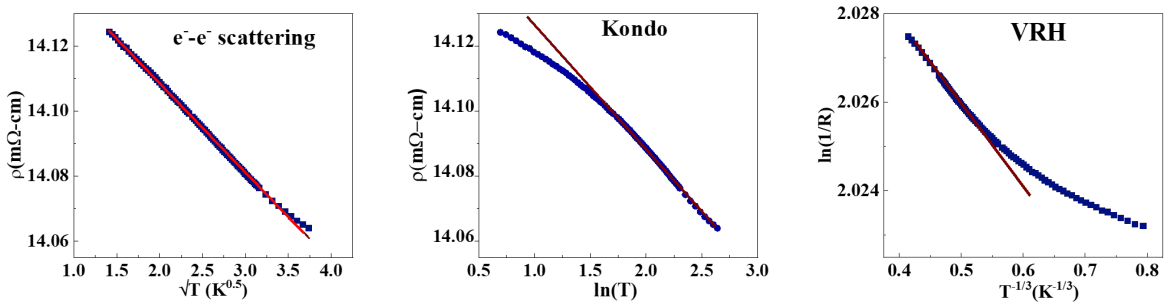

(a) (b) (c)

Figure 5.4: Analysis of resistivity data to identify potential mechanisms responsible for the observed increase in resistivity; (a) fitting of the data into -$\sqrt{T}$ dependence (EEI); (b) fitting of the data into ln(T) behavior (kondo); (c) fitting of the data into variable range hopping model in 2D. The line acts as a guide to the eye to observe deviations from linear behavior.

In the presence of a magnetic field, measurements of resistivity reveal a shift of the temperature minima to lower values (H = 1 T, T_{min} = 12 K, H = 2 T, T_{min} = 9 K). This observation suggests a significant Kondo contribution to the resistivity upturn, as a contribution from EEI is comparatively insensitive to the magnetic field. However, for H = 4 T and H = 6 T, the minima in

resistivity are observed at 6.5 K and 6 K, respectively; the non-vanishing minima further suggest the contribution due to inelastic electron-electron scattering. Moreover, when the superposition of -ln(T) and -$\sqrt{T}$ is used to fit the resistivity data, the coefficient of ln(T) term was observed to be one order smaller than that of -$\sqrt{T}$. Therefore, from the above analysis, it is plausible to assume that the upturn has contribution from both the phenomena.

5.4 $Cr_{0.45}ZrTe_2$

Figure 5.5 displays the resistivity data for the sample $Cr_{0.45}ZrTe_2$ for temperature ranges 77 K - 296 K (a) and 300 K - 385 K (b). These data are collected in our home-built set-ups. A divergence of resistivity values for the heating cycle and cooling cycle is observed near 290 K. Note that thermal hysteresis is also a characteristic of CDW transitions, although many times, directional strain or bad sample quality can also lead to differences in heating and cooling resistivity values. Therefore, measurements were conducted on multiple samples to ensure that the observed deviation is not an experimental artifact. Additionally, the quality of the samples was assessed using X-ray diffraction (XRD). To further investigate the transport properties, resistivity measurements were taken at temperatures above room temperature. An anomaly is observed in the resistivity around 360 K during both the heating and cooling cycles, accompanied by a large hysteresis; however, additional measurements are needed to confirm the existence of this anomaly. To further characterize the samples, we plan to perform high-temperature powder X-ray diffraction (PXRD) to determine whether a structural transition is observed.

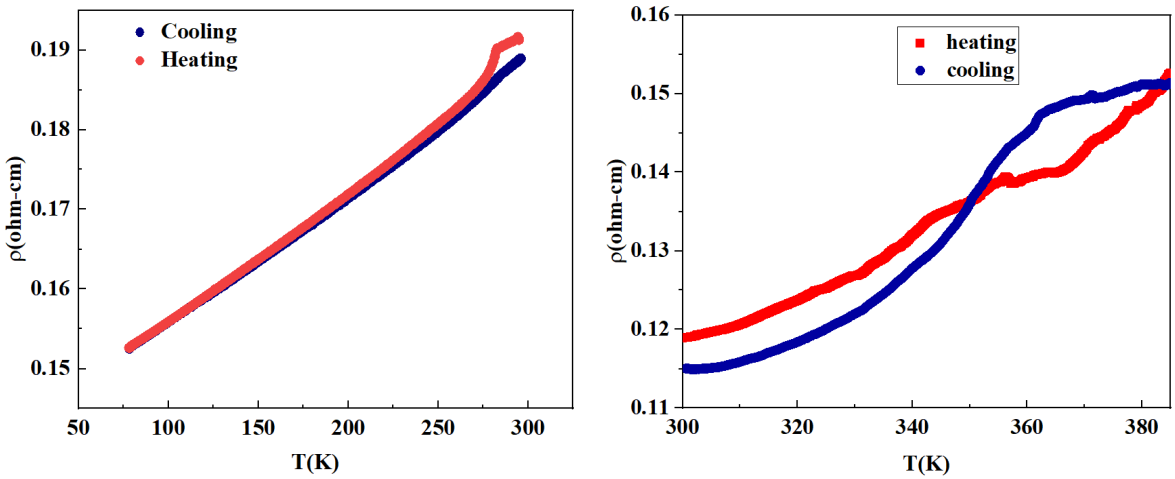

Figure 5.5: Temperature dependent resistivity data for $Cr_{0.45}ZrTe_2$; (a) in temperature range 77 K - 295 K; (b) in temperature range 300 K - 385 K

Conclusions

As part of this thesis, we built a low-temperature resistivity measurement setup and validated its performance. This setup allows for precise transport measurements in the 4.3 K to 295 K range, crucial for characterizing phase transitions of the materials studied as a part of the thesis work. Validation against known materials ($TiSe_2$, Pb, and Nb) confirms the reliability of the setup. The set-up is designed to measure two samples simultaneously and features a user-friendly interface. For instance, samples can be easily loaded or unloaded by detaching the sample holder from the sample probe using low-temperature PEEK connectors. This allows the sample holder to be placed under a light microscope for making electrical contacts on small samples. A distinctive advantage of this set-up is that it eliminates the need for an external temperature controller—temperature is instead varied by moving the sample probe into or out of the storage dewar in a controlled manner using a stepper motor. The translation speed of the probe can be precisely controlled, which directly determines the cooling or heating rate. Since the temperature evolution is unidirectional (i.e., the sample is either monotonically cooled or heated depending on the direction of probe movement), the system is particularly well-suited for capturing hysteretic transitions.

As part of the thesis, we have successfully performed crystal growth of the Cr_xZrTe_2 (where $x = 0.25, 0.30, 0.40, 0.45$) using the oscillating chemical vapor transport (OCVT) method, optimized growth parameters for each x value to obtain high-quality single crystals characterized using, PXRD, EDS, and chemical mapping. The successful growth of the single crystals allowed us to carry out transport studies of these systems, leading to new insights into the physical properties of these systems. The Cr_xZrTe_2 systems all exhibit a metallic trend in resistivity. However, interesting behaviors arise at low temperatures when the x value is varied.

We demonstrate that the transport properties of Cr-intercalated ZrTe2 are highly sensitive to the level of intercalation. Depending on the amount of intercalated Cr, we observe a variety of intriguing resistivity behaviors. For example, a sharp drop in resistivity occurs in $Cr0.25ZrTe_2$ below 4 K, which we initially attributed to the onset of superconductivity. However, measurements conducted in the presence of a magnetic field not only reveal the complete suppression of this resistivity anomaly but also show a significant negative magnetoresistance (MR) over a wide temperature range. This suggests that the magnetic Cr ions play a key role in the observed

behavior. While it is possible that the resistivity drop is non-superconducting and instead related to spin-glass freezing of the Cr moments, magnetic susceptibility measurements are required to confirm this hypothesis.

When the intercalation level is raised to 40%, the resistivity behavior at low temperatures changed dramatically: instead of a sharp drop seen for x = 0.25, at x = 0.45, an upturn is observed in the low-temperature resistivity below T = 15 K, which is best explained by contribution from both Kondo behavior and weak localization due to inelastic electron-electron scattering. However, for a definitive conclusion, further studies are required. For $Cr_{0.45}ZrTe_2$, a thermal hysteresis is observed near Room temperature, possibly due to a CDW-type transition. Currently, we are performing further characterizations to understand the cause of the hysteresis.

In future, for an accurate determination of the structure of these materials should be carried out to understand how the intercalated Cr ions are arranged between the van der Waals layers.Due to the availability of single crystals, angle-resolved photoemission spectroscopy can be performed to assess the changes in the electronic structure upon Cr intercalation. Moreover, understanding how intercalation influences the electronic and magnetic properties of $ZrTe_2$ and how it differs from other intercalated MX_2 (M = Zr, Ti, X = S, Se, Te) will provide valuable guidance for designing materials with tailored functionalities.

References

[1] Seung-Ho Baek et al. “Interplay of charge density waves, disorder, and superconductivity in 2H-TaSe2 elucidated by NMR”. In: *New Journal of Physics* 24.4 (2022), p. 043008. DOI: 10.1088/1367-2630/ac5eec. URL: https://dx.doi.org/10.1088/1367-2630/ac5eec.

[2] N V Baranov et al. “Ferromagnetism and structural transformations caused by Cr intercalation into TiTe2”. In: *Journal of Physics: Condensed Matter* 21.50 (2009), p. 506002. DOI: 10.1088/0953-8984/21/50/506002. URL: https://dx.doi.org/10.1088/0953-8984/21/50/506002.

[3] Bruker. *Bruker D8 Advance Powder X-ray Diffractometer*. Accessed: 2024-04-04. URL: https://hijaz-jo.com/product/the-d8-advance-family/.

[4] I. A. Campbell, P. J. Ford, and A. Hamzi ć. “Resistivity of spin-glasses”. In: *Phys. Rev. B* 26 (9 1982), pp. 5195–5206. DOI: 10.1103/PhysRevB.26.5195. URL: https://link.aps.org/doi/10.1103/PhysRevB.26.5195.

[5] H. Cercellier et al. “Evidence for an Excitonic Insulator Phase in $1T-TiSe_2$”. In: *Phys. Rev. Lett.* 99 (14 2007), p. 146403. DOI: 10.1103/PhysRevLett.99.146403. URL: https://link.aps.org/doi/10.1103/PhysRevLett.99.146403.

[6] Lucas E. Correa et al. “Evidence for multiband superconductivity and charge density waves in Ni-doped ZrTe2”. In: *Journal of Alloys and Compounds* 907 (2022), p. 164477. ISSN: 0925-8388. DOI: https://doi.org/10.1016/j.jallcom.2022.164477. URL: https://www.sciencedirect.com/science/article/pii/S0925838822008684.

[7] Lucas E. Correa et al. “Growth of pure and intercalated ZrTe2, TiTe2 and HfTe2 dichalcogenide single crystals by isothermal chemical vapor transport”. In: *Journal of Crystal Growth* 595 (2022), p. 126819. ISSN: 0022-0248. DOI: https://doi.org/10.1016/j.jcrysgro.2022.126819.

[8] S.O. Ferreira. *Advanced Topics on Crystal Growth*. IntechOpen, 2013. ISBN: 9789535163077.

[9] Marc Gabay and Gérard Toulouse. “Coexistence of Spin-Glass and Ferromagnetic Orderings”. In: *Phys. Rev. Lett.* 47 (3 1981), pp. 201–204. DOI: 10.1103/PhysRevLett.47.201. URL: https://link.aps.org/doi/10.1103/PhysRevLett.47.201.

[10] George Gruner. *Density waves in solids*. Addison-Wesley Publishing Company, 1994.

[11] Gang Hee Han et al. "van der Waals Metallic Transition Metal Dichalcogenides". In: *Chemical Reviews* 118.13 (2018). PMID: 29957928, pp. 6297–6336. DOI: 10.1021/acs.chemrev.7b00618. eprint: https://doi.org/10.1021/acs.chemrev.7b00618. URL: https://doi.org/10.1021/acs.chemrev.7b00618.

[12] H P Hughes. "Structural distortion in TiSe2 and related materials-a possible Jahn-Teller effect?" In: *Journal of Physics C: Solid State Physics* 10.11 (1977), p. L319. DOI: 10.1088/0022-3719/10/11/009. URL: https://dx.doi.org/10.1088/0022-3719/10/11/009.

[13] Indrani Kar et al. "Metal-chalcogen bond-length induced electronic phase transition from semiconductor to topological semimetal in ZrX_2 (X = Se and Te)". In: *Phys. Rev. B* 101 (16 Apr. 2020), p. 165122. DOI: 10.1103/PhysRevB.101.165122.

[14] J. Laverock et al. "k-resolved susceptibility function of $2H$-$TaSe_2$ from angle-resolved photoemission". In: *Phys. Rev. B* 88 (3 2013), p. 035108. DOI: 10.1103/PhysRevB.88.035108. URL: https://link.aps.org/doi/10.1103/PhysRevB.88.035108.

[15] Zefang Li et al. "Thermodynamics and Kinetics Synergy for Controlled Synthesis of 2D van der Waals Single-Crystal NbSe2 via Modified Chemical Vapor Transport". In: *Crystal Growth & Design* 20.2 (2020), pp. 706–712. DOI: 10.1021/acs.cgd.9b01131. URL: https://doi.org/10.1021/acs.cgd.9b01131.

[16] Eric J. Mittemeijer and Udo Welzel. In: *Zeitschrift für Kristallographie* 223.9 (2008), pp. 552–560. DOI: doi:10.1524/zkri.2008.1213. URL: https://doi.org/10.1524/zkri.2008.1213.

[17] Zahir Muhammad et al. "Lattice dynamics, optical and thermal properties of quasi-two-dimensional anisotropic layered semimetal ZrTe2". In: *Inorg. Chem. Front.* 8 (16 2021), pp. 3885–3892. DOI: 10.1039/D1QI00553G. URL: http://dx.doi.org/10.1039/D1QI00553G.

[18] Hidden Order and Dimensional Crossover of the Charge Density Waves in TiSe2. "Chen P, Chan YH, Fang XY, Mo SK, Hussain Z, Fedorov AV, Chou MY, Chiang TC". In: *Sci Rep.* 99 (14 2016), p. 146403. DOI: 10.1103/PhysRevLett.99.146403. URL: https://link.aps.org/doi/10.1103/PhysRevLett.99.146403.

[19] W. B. Pearson and I. M. Templeton. "Superconducting Transition of Lead". In: *Phys. Rev.* 109 (4 1958), pp. 1094–1094. DOI: 10.1103/PhysRev.109.1094. URL: https://link.aps.org/doi/10.1103/PhysRev.109.1094.

[20] R.E. Peierls. *Quantum theory of solids*. Vol. 126. Oxford University press, 1955.

[21] Korolev Pleshchev and Dorofeev. “Magnetic state of intercalation compounds in the CrxTiTe2 system”. In: *Phys. Solid State* 46 (3 2004), pp. 289–293. DOI: doi.org/10.1134/1.1649426.

[22] ResearchGate. *Another beauty of analytical chemistry: chemical analysis of inorganic pigments of art and archaeological objects*. Scientific Figure on ResearchGate. Available from: https://www.researchgate.net/figure/Scheme-of-a-X-ray-powder-diffraction-instrument-with-Bragg-Brentano-geometry_fig38_307091318 [accessed 4 Apr 2025]. 2025.

[23] P L Rossiter. “Effects of co-existing atomic and magnetic clustering on electrical resistivity: Cu-Ni alloys”. In: *Journal of Physics F: Metal Physics* 11.10 (1981), p. 2105. DOI: 10.1088/0305-4608/11/10/021. URL: https://dx.doi.org/10.1088/0305-4608/11/10/021.

[24] A.S. Shkvarin et al. “The crystal structure, chemical bonding, and magnetic properties of the intercalation compounds CrxZrTe2 (x = 0–0.3)”. In: *Materials Science and Engineering: B* 270 (2021), p. 115218. ISSN: 0921-5107. DOI: https://doi.org/10.1016/j.mseb.2021.115218. URL: https://www.sciencedirect.com/science/article/pii/S0921510721001781.

[25] Cengiz Temiz. “Scanning Electron Microscopy”. In: *Electron Microscopy*. Ed. by Mohsen Mhadhbi. Rijeka: IntechOpen, 2022. Chap. 1. DOI: 10.5772/intechopen.103956. URL: https://doi.org/10.5772/intechopen.103956.

[26] Polychronis Tsipas et al. “Massless Dirac Fermions in ZrTe2 Semimetal Grown on InAs(111) by van der Waals Epitaxy”. In: *ACS Nano* 12.2 (2018). PMID: 29314824, pp. 1696–1703. DOI: 10.1021/acsnano.7b08350. URL: https://doi.org/10.1021/acsnano.7b08350.

[27] Le Van Khoi et al. “Spin glass behavior and colossal negative magnetoresistance of the $p-Zn_{1-x}Mn_xTe$ strongly doped with phosphorus”. In: *Phys. Rev. B* 101 (5 2020), p. 054440. DOI: 10.1103/PhysRevB.101.054440. URL: https://link.aps.org/doi/10.1103/PhysRevB.101.054440.

[28] V. Vescoli et al. “Dynamics of Correlated Two-Dimensional Materials: The $2H - TaSe_2$ Case”. In: *Phys. Rev. Lett.* 81 (2 1998), pp. 453–456. DOI: 10.1103/PhysRevLett.81.453. URL: https://link.aps.org/doi/10.1103/PhysRevLett.81.453.

[29] Yihao Wang et al. “Weak Kondo effect in the monocrystalline transition metal dichalcogenide $ZrTe_2$”. In: *Phys. Rev. B* 103 (17 2021), p. 174418. DOI: 10.1103/PhysRevB.103.174418. URL: https://link.aps.org/doi/10.1103/PhysRevB.103.174418.

[30] G. W. Webb. “Low-Temperature Electrical Resistivity of Pure Niobium”. In: *Phys. Rev.* 181 (3 1969), pp. 1127–1135. DOI: 10.1103/PhysRev.181.1127. URL: https://link.aps.org/doi/10.1103/PhysRev.181.1127.

[31] F. Weber et al. “Extended Phonon Collapse and the Origin of the Charge-Density Wave in 2H-NbSe2”. In: *Phys. Rev. Lett.* 107 (10 2011), p. 107403. DOI: 10.1103/PhysRevLett.107.107403. URL: https://link.aps.org/doi/10.1103/PhysRevLett.107.107403.

[32] A. Wegner et al. “Evidence for pseudo–Jahn-Teller distortions in the charge density wave phase of $1T-TiSe_2$”. In: *Phys. Rev. B* 101 (19 2020), p. 195145. DOI: 10.1103/PhysRevB.101.195145. URL: https://link.aps.org/doi/10.1103/PhysRevB.101.195145.

[33] E. J. Woll and W. Kohn. “Images of the Fermi Surface in Phonon Spectra of Metals”. In: *Phys. Rev.* 126 (5 1962), pp. 1693–1697. DOI: 10.1103/PhysRev.126.1693. URL: https://link.aps.org/doi/10.1103/PhysRev.126.1693.

[34] Bo Zhang et al. “Electronic Structures of Cr-Intercalated ZrTe2 Revealed by Angle-Resolved Photoemission Spectroscopy”. In: *The Journal of Physical Chemistry C* 124.30 (2020), pp. 16561–16567. DOI: 10.1021/acs.jpcc.0c04168. URL: https://doi.org/10.1021/acs.jpcc.0c04168.

[35] Bo Zhang et al. “Electronic Structures of Cr-Intercalated ZrTe2 Revealed by Angle-Resolved Photoemission Spectroscopy”. In: *The Journal of Physical Chemistry C* 124.30 (2020), pp. 16561–16567. DOI: 10.1021/acs.jpcc.0c04168. URL: https://doi.org/10.1021/acs.jpcc.0c04168.

[36] J Zhao et al. “Spectroscopic study of the charge density wave order in 2H-TaS2”. In: *Spintronics X*. Vol. 10357. SPIE. 2017, pp. 47–54.

[37] Xuetao Zhu et al. “Misconceptions associated with the origin of charge density waves”. In: *Advances in Physics: X* 2.3 (2017), pp. 622–640. DOI: 10.1080/23746149.2017.1343098. URL: https://doi.org/10.1080/23746149.2017.1343098.